Supporting Information

Boosting Electrocatalytic Performance of NiFe Layered Double Hydroxides by Exposing High Active Edge Plane (012) for Oxygen Evolution Reaction

Jia-Wei Zhao†, Zi-Xiao Shi†, Cheng-Fei Li, Lin-Fei Gu, and Gao-Ren Li*

MOE Laboratory of Bioinorganic and Synthetic Chemistry, The Key Lab of Low-carbon Chemistry & Energy Conservation of Guangdong Province, School of Chemistry, Sun Yat-sen University, Guangzhou 510275, China

E-mail: ligaoren@mail.sysu.edu.cn

Evaluation of OER Activity. The OER free energy profiles were derived using the same scheme utilized in previous studies. The free energy change of any elementary step that involves the production of a proton-electron pair will decrease linearly with applied potential versus the RHE:

$$\Delta G = \Delta G^{o} - eU_{\mathrm{RHE}}$$

The theoretical overpotential at which the step becomes downhill may be calculated as:

$$\eta = \frac{max(\Delta G_1, \Delta G_2, \Delta G_3, \Delta G_4)}{e} - 1.23\ [V]$$

The adsorbate evolution mechanism (AEM) contains four elementary steps, and each of these steps contains a single proton-electron transfer, shown as the following:

$$* + H_2O \rightarrow HO* + e^- + H^+$$

$$HO* \rightarrow O* + e^- + H^+$$

$$O* + H_2O \rightarrow HOO* + e^- + H^+$$

$$HOO* \rightarrow * + O_2 + e^- + H^+$$

The free energy of each adsorbate is calculated at 0 V *vs* RHE by referencing to liquid water and hydrogen gas at standard conditions. The correction calculated using the harmonic approximation for every adsorbate and surface, with typical values of +0.05 eV, +0.35 eV, +0.40 eV for O*, HO* and HOO*, respectively.

Bode Diagram. It is typical for α-Ni(OH)$_2$ (and its corresponding LDHs) to electrochemically oxidized into (metal-doped) γ-NiOOH by losing the protons in the hydoxyles and remaining the layered structure under OER condition as the following:

$$\alpha\text{-Ni(Fe)(OH)}_2 \underset{\longleftarrow}{\overset{\text{electrochemical}}{\longrightarrow}} \gamma\text{-Ni(Fe)OOH}$$

So the NiFe LDHs, which can also be expressed as Fe-doped α-Ni(OH)$_2$, is oxidized into Fe-doped γ-NiOOH (Fe-γ-NiOOH), which is the true active materials under OER condition. And all the theoretical investigations are conducted with γ-NiOOH and Fe-γ-NiOOH. The model of γ-NiOOH we use here is a modified model proposed by Ceder and Goddard,[1] with 1/3 of the Ni atoms (those close to Na^+ ions) have the oxidation of +3. Thus the rest 2/3 of Ni atoms have oxidation states of +4, leading to an average oxidation state of +3.67 for Ni, in agreement with experimental reports. The Fe doping is by substituting a Ni atom of +4 oxidation state.

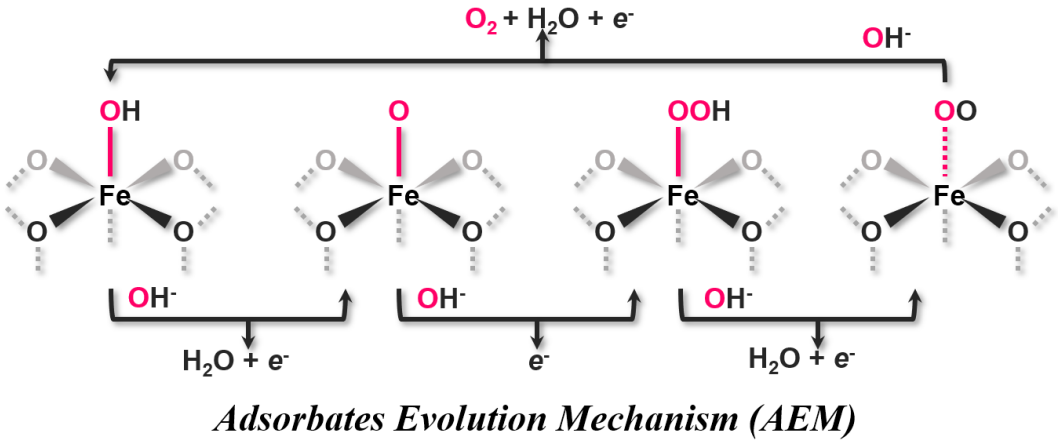

Figure S1. Simulated OER mechanisms: the adsorbate evolution mechanism (AEM), in which the atoms of the catalysis surface do not participate in the formation of oxygen.

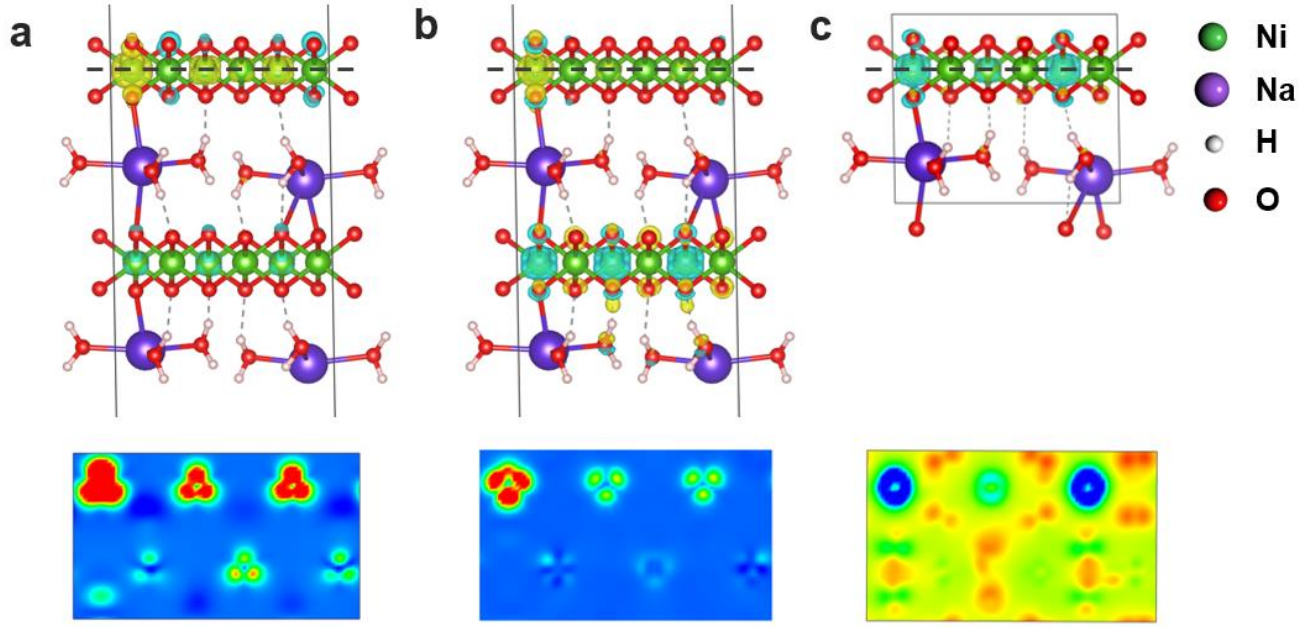

Figure S2. Calculated electronics of (003) surface of γ-NiOOH. (a) the charge density difference on γ-NiOOH: $\rho = \rho[\gamma\text{-NiOOH}] - \rho_{top}[NiO_6 + water] - \rho_{bottom}[NiO_6 + water]$; Yellow and cyan iso-surface represents electron accumulation and electron depletion, respectively; (b) the charge density difference on γ-NiOOH: $\rho = \rho[\gamma\text{-NiOOH}] - \rho_{top}[NiO_6] - \rho_{top}[water] - \rho_{bottom}[NiO_6] - \rho_{bottom}[water]$; (c) the charge density difference on unit cell with iso-surface 2D view.

It is clear from (a), (b) and (c) that the electron transfer exists between the upper and lower layer, which lowers the valence state of Ni atoms on the upper layer.

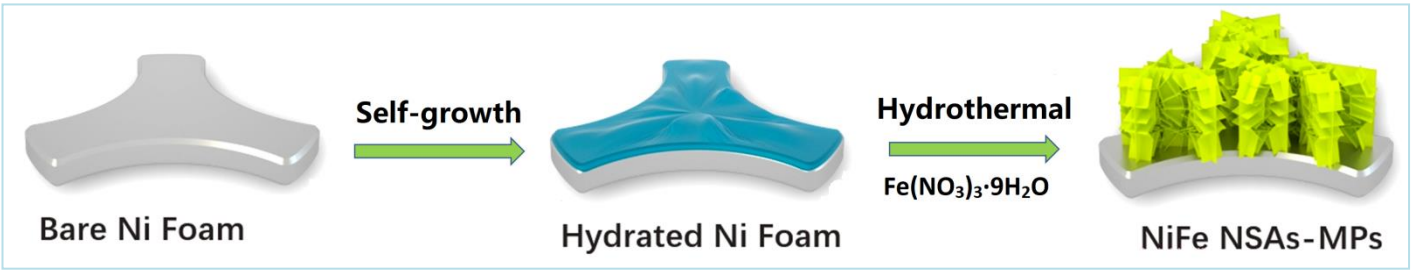

Figure S3. The illustration of the synthesis process of NiFe NSAs-MPs.

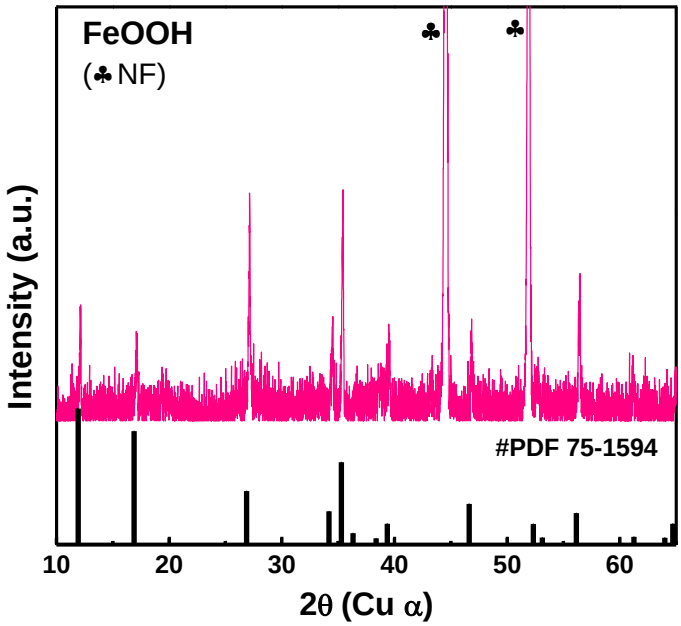

Figure S4. XRD pattern of the synthesized β-FeOOH.

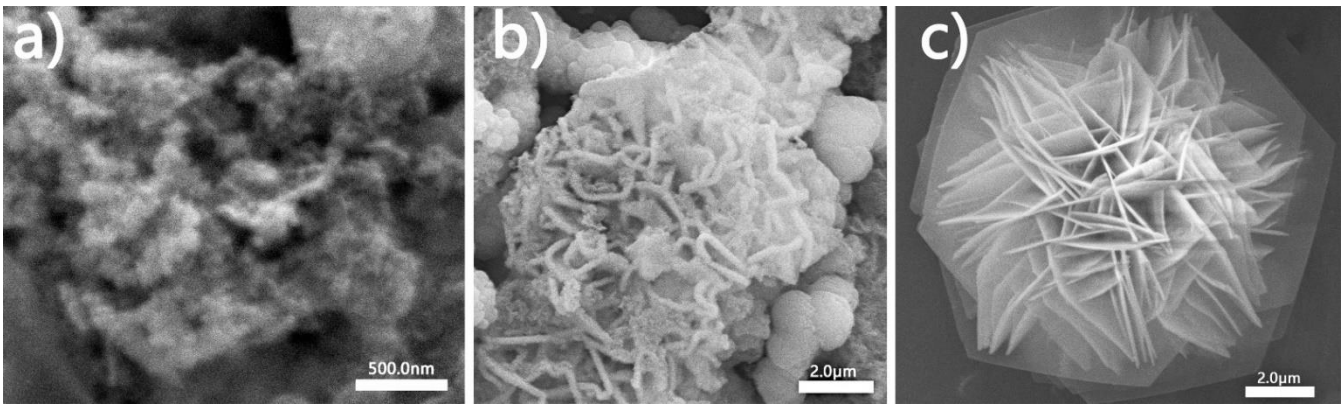

Figure S5. The growing process of NiFe NSAs-MPs by changing the reaction time at 120 ℃: (a) for 0 min, (b) 60 min, and (c) 5 h.

The dissolution-recrystallization growth of NiFe NSAs-MPs is investigated by changing the hydrothermal reaction time. When the reaction time is from 0 to 60 min, the shape of NiFe NSAs-MPs gradually emerges, and the nanosheets grow simultaneously with the microplate, indicating the intensive nucleating density of NiFe nanosheets on the microplate. Finally, after 5 h the NSAs-MPs have a rather constant shape and are used as the target product since longer reaction time would lead to a higher crystalline degree and thus will hamper OER performance.[8]

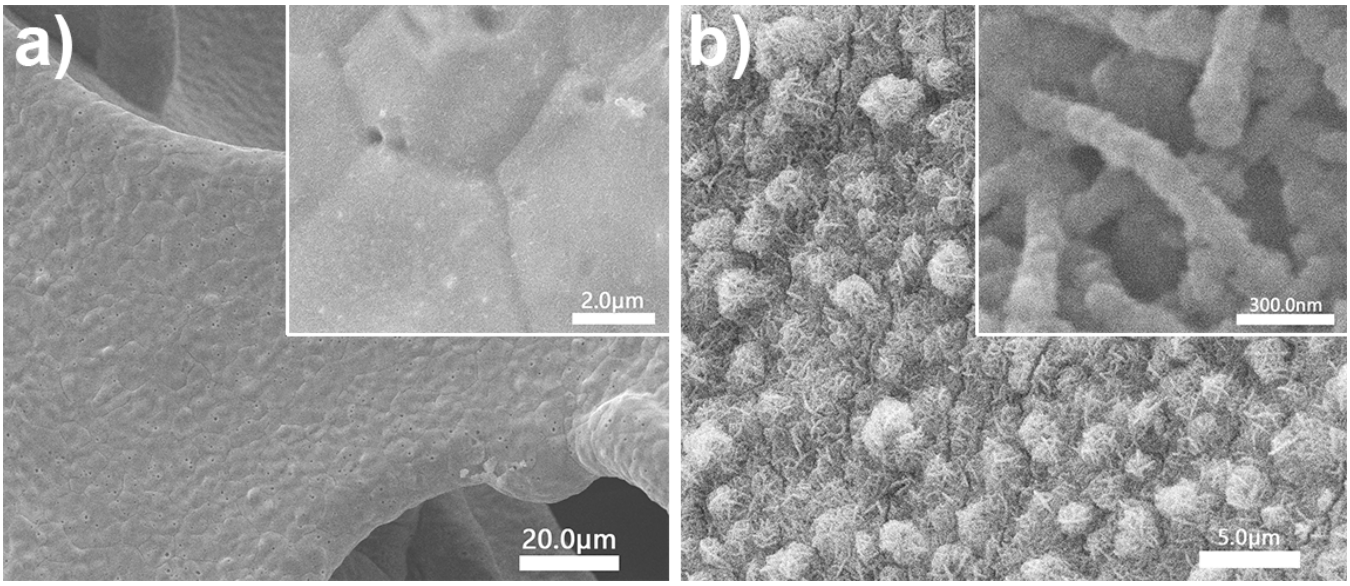

Figure S6. SEM images of (a) bare NF, (b) the hydrated NF (inset images are the enlarged pictures).

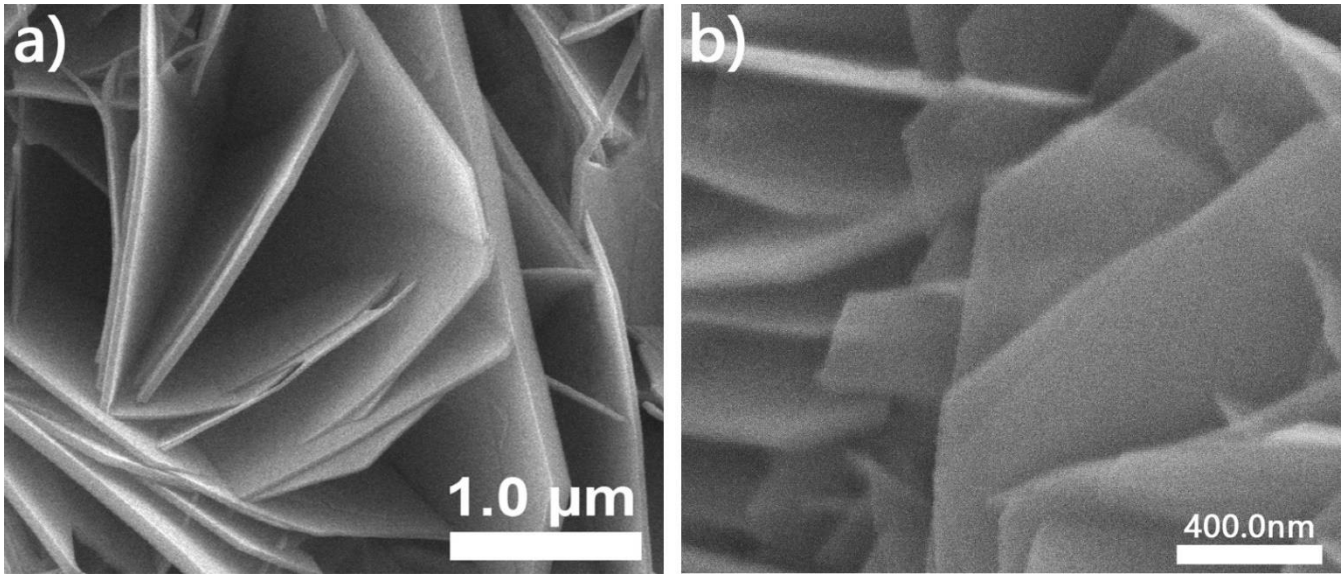

Figure S7. SEM images of NiFe MSAs with different magnifications.

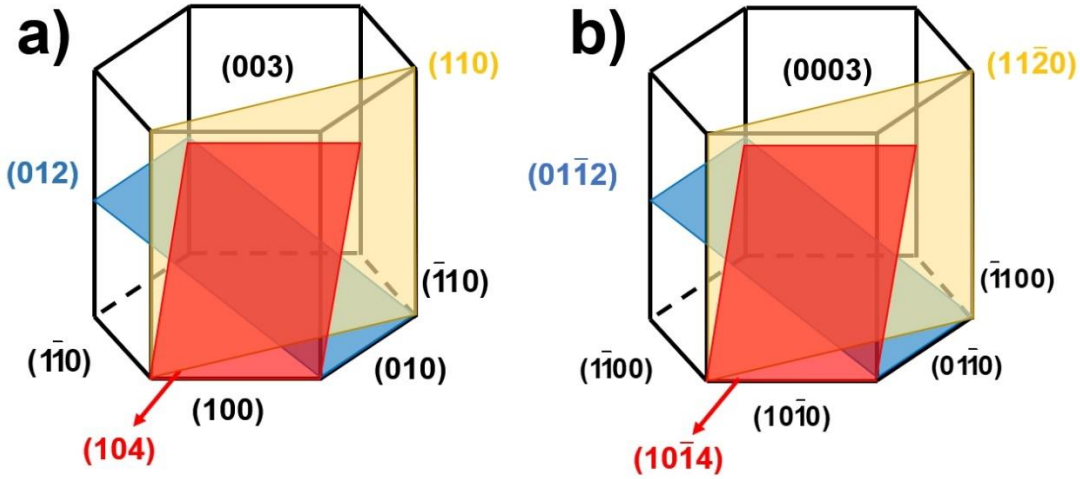

Figure S8. The schematic illustration of a unit cell of NiFe NSAs-MPs from (a) Miller indices (three-index system) and (b) Bravais indices (four-index system). The Miller indices with three lattice vectors and the Bravais system with four indices both are suitable to describe a hexagonal lattice, as in the layered (oxy)hydroxides.

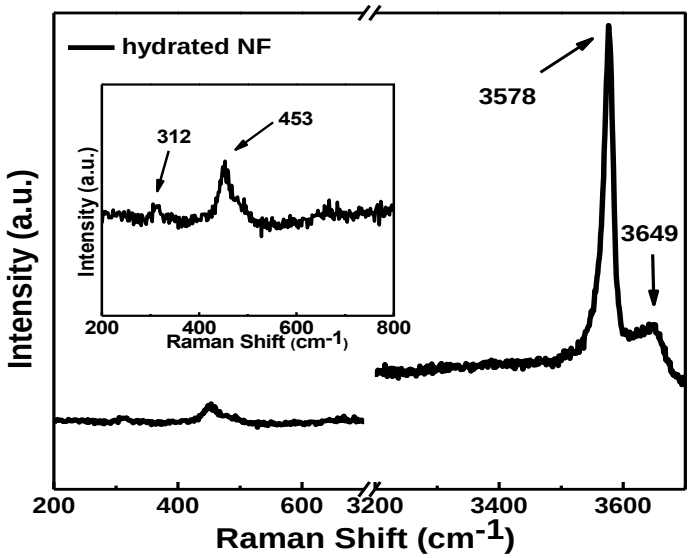

Figure S9. Raman spectra of the hydrated NF (the inset is the partially enlarged graph).

The peaks at 312 and 453 cm^{-1} and the strong peak at 3578 cm^{-1} are well assigned to β-$Ni(OH)_2$ phase. A weak peak at 3649 can be assigned to α-$Ni(OH)_2$, indicating that a small amount of α-$Ni(OH)_2$ exists in the sample.[2, 3] According to the previous study, the formed $Ni(OH)_2$ layer on Ni foam (NF) is "bad-crystalline" β-$Ni(OH)_2$ phase.[4, 5]

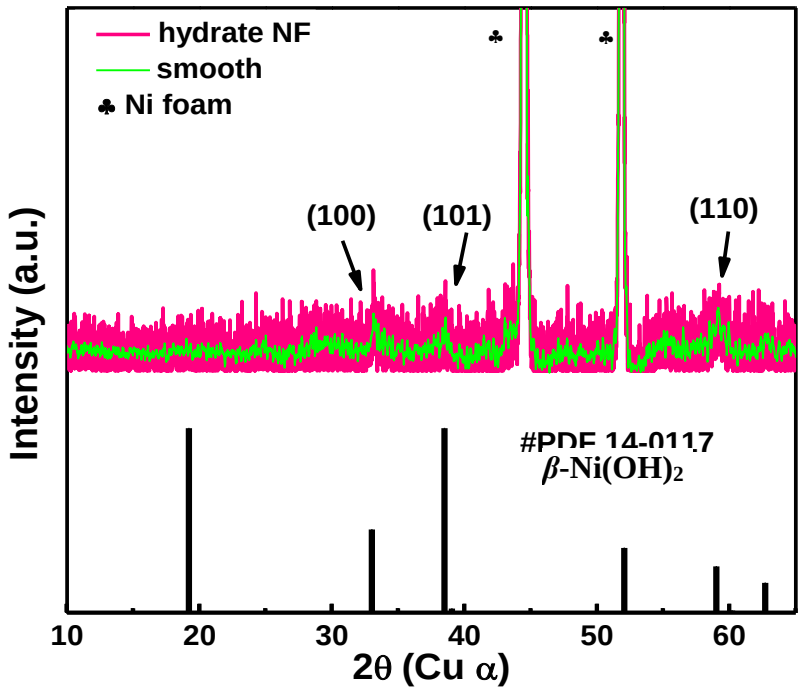

Figure S10. XRD pattern of the hydrated NF (the green line is the smoothing pattern of the original data with the points of window index of 20).

Here the results of XRD shows that the formed β-$Ni(OH)_2$ layer on Ni foam is "bad-crystalline" phase, which is in accord with the Raman spectra (Figure S9).

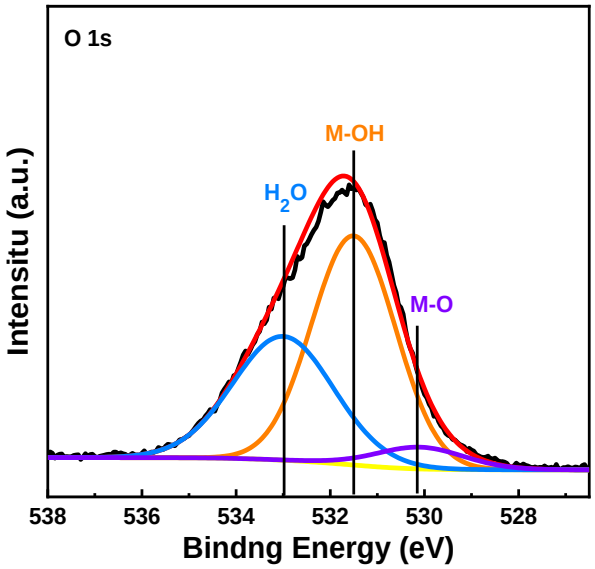

Figure S11. XPS spectra of O 1s a of NiFe NSAs-MPs.

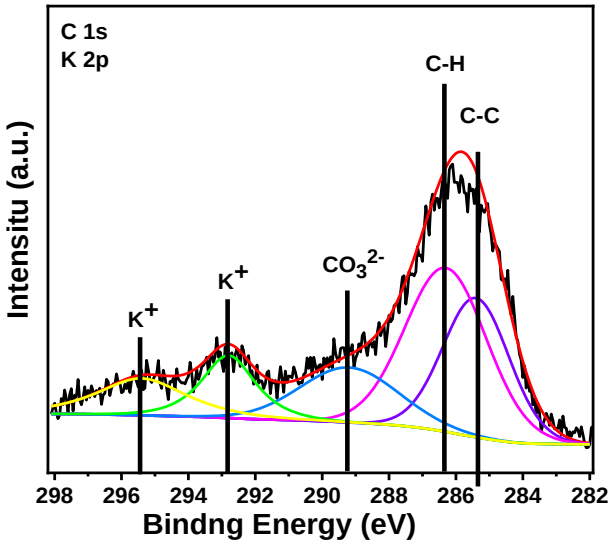

Figure S12. XPS spectra of C 1s and K 2p of NiFe NSAs-MPs.

X-ray photoelectron spectra (XPS) of O 1s region of NiFe NSAs-MPs can be distinguished into three bands: metal-oxide (530.1 eV), metal-hydroxyl (531.5 eV) and intercalated H_2O (533.1 eV) as shown in Figure S8c, which is well assigned to O 1s spectrum of the hydroxides. The C1s-K2p XPS spectra of NiFe NSAs-MPs show the signals of K^+ and CO_3^{2-} after stabilizing the NiFe NSAs-MPs in KOH (Figure S8d).[6-8]

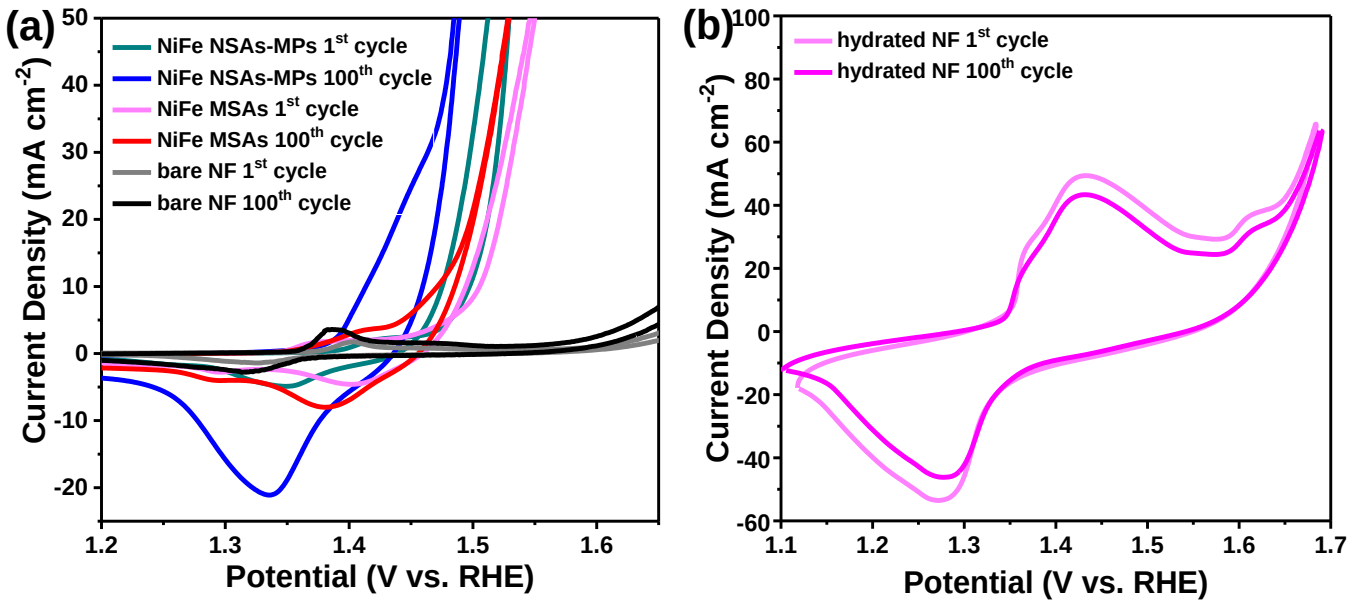

Figure S13. (a) The 1st and 100th cycles of CVs of NiFe NSAs-MPs, NiFe MSAs, and bare NF; (b) The 1st and 100th cycles of CVs of hydrated NF.

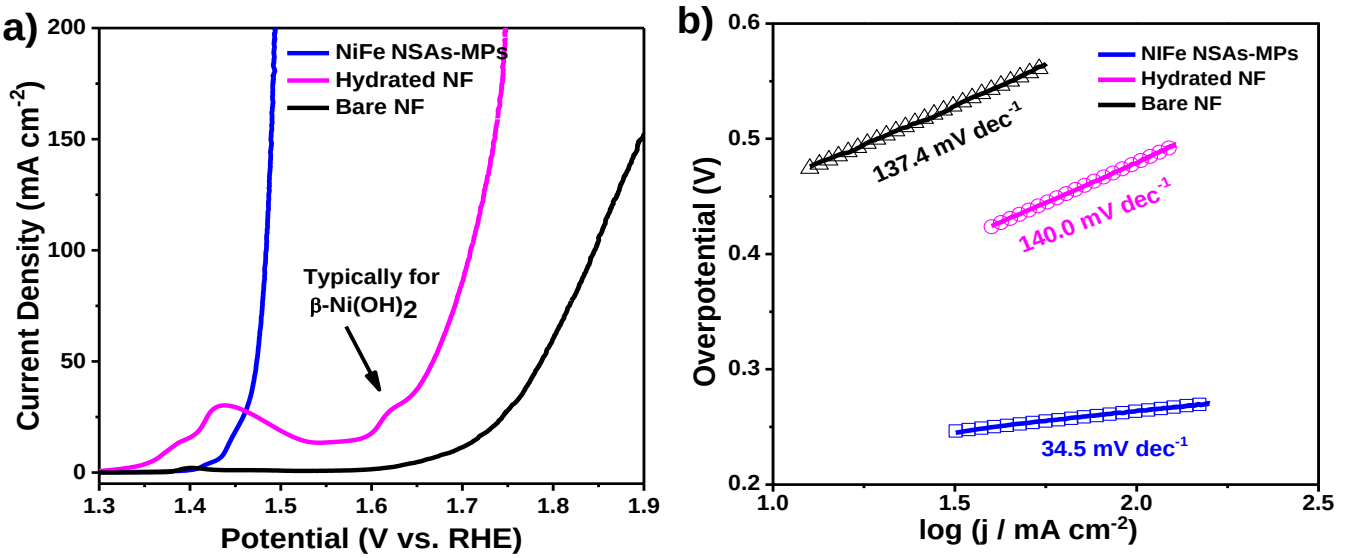

Figure S14. (a) LSVs of NiFe NSAs-MPs, hydrated NF, and bare NF before activation; (b) Tafel slopes derived from LSVs of NiFe NSAs-MPs, hydrated NF, and bare NF.

The polarization curve of the hydrated NF shows a second oxidation peak before OER, which is a typical electrochemical characteristic of β-$Ni(OH)_2$,[9] in accord with Raman and XRD patterns of hydrated NF.

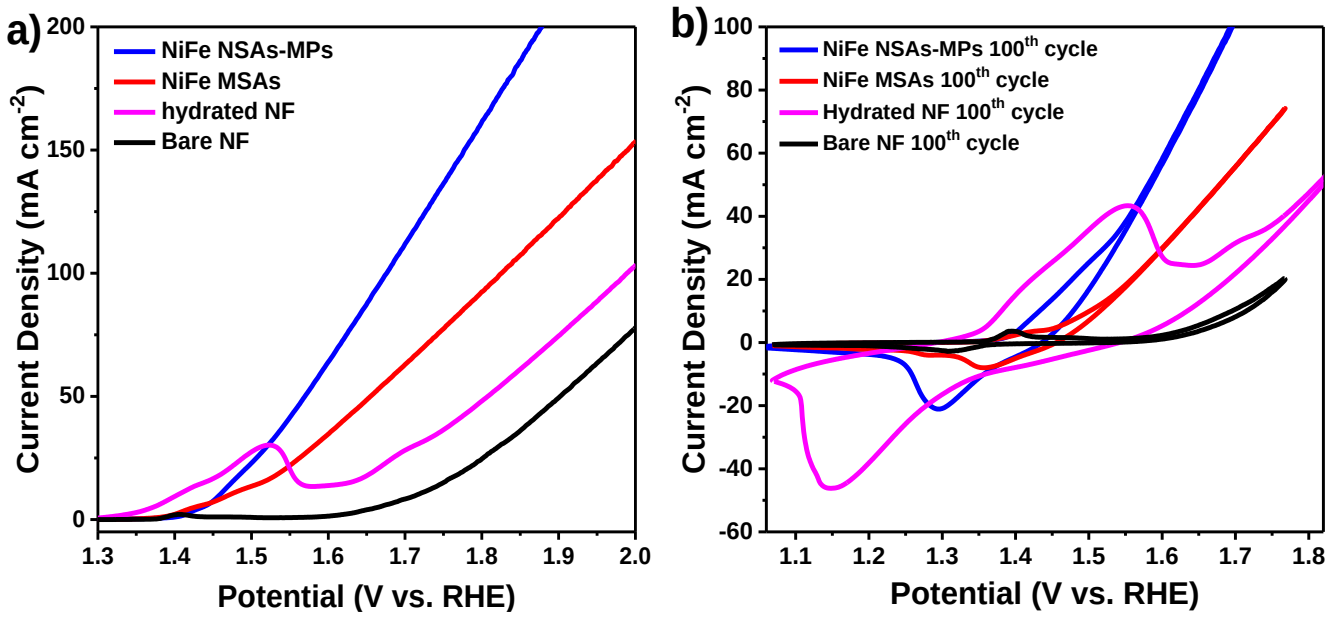

Figure S15. (a) LSVs and (b) the 100th CVs of NiFe NSAs-MPs, NiFe MSAs, hydrated NF, and bare NF without IR compensation.

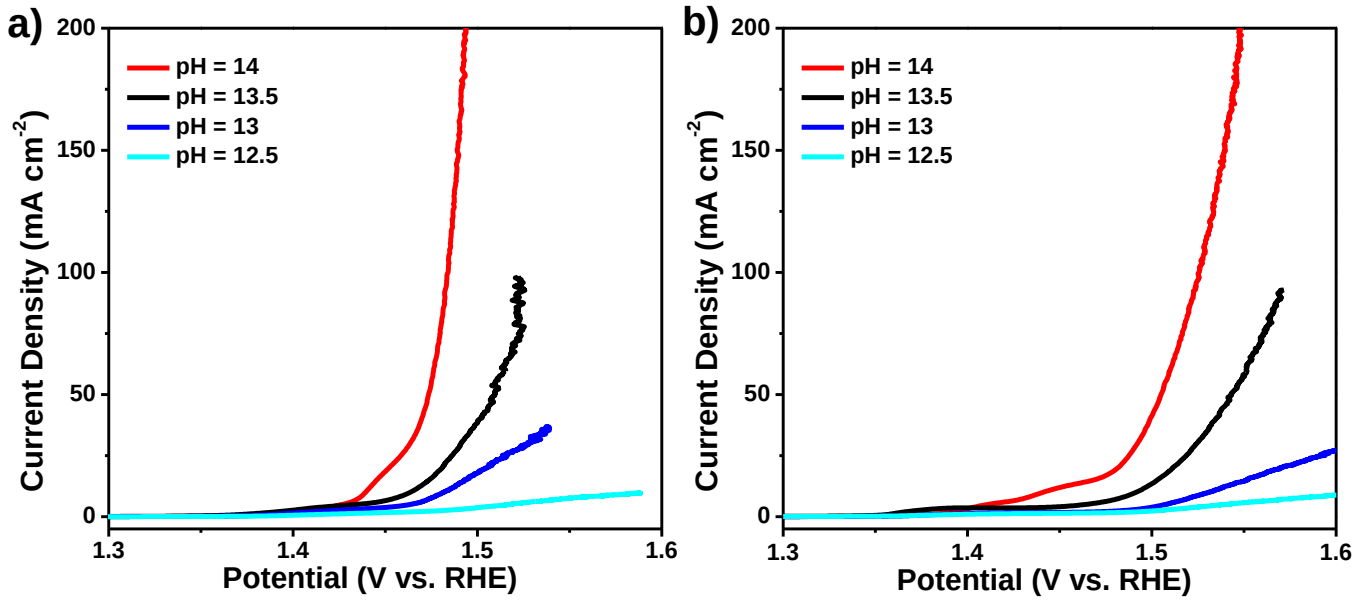

Figure S16. LSVs of (a) NiFe NSAs-MPs and (b) NiFe MSAs at different pH values in KOH solutions. The result shows the OER performances of both NiFe NSAs-MPs and NiFe MSAs highly depend on the pH value.

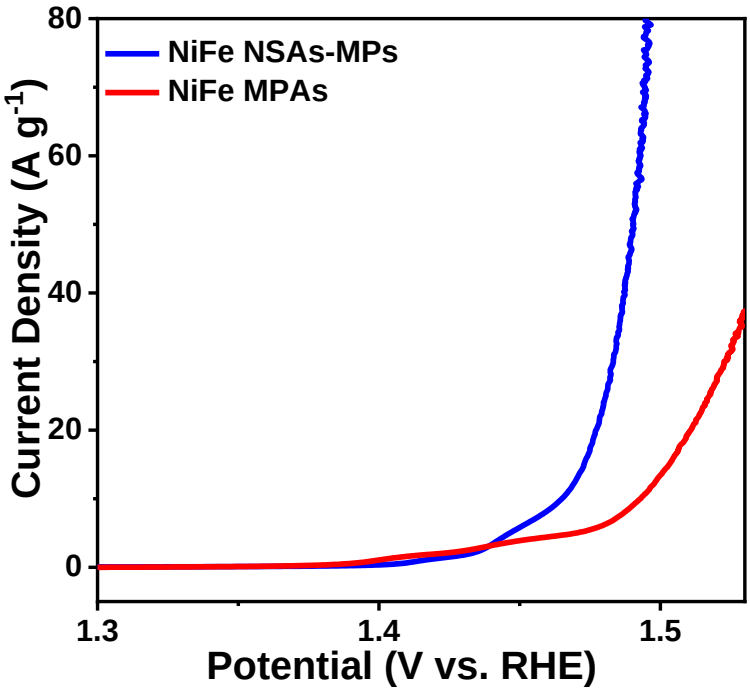

Figure R17. LSVs of NiFe NSAs-MPs and NiFe MSAs in Figure 5a in the paper are normalized by mass of catalysts.

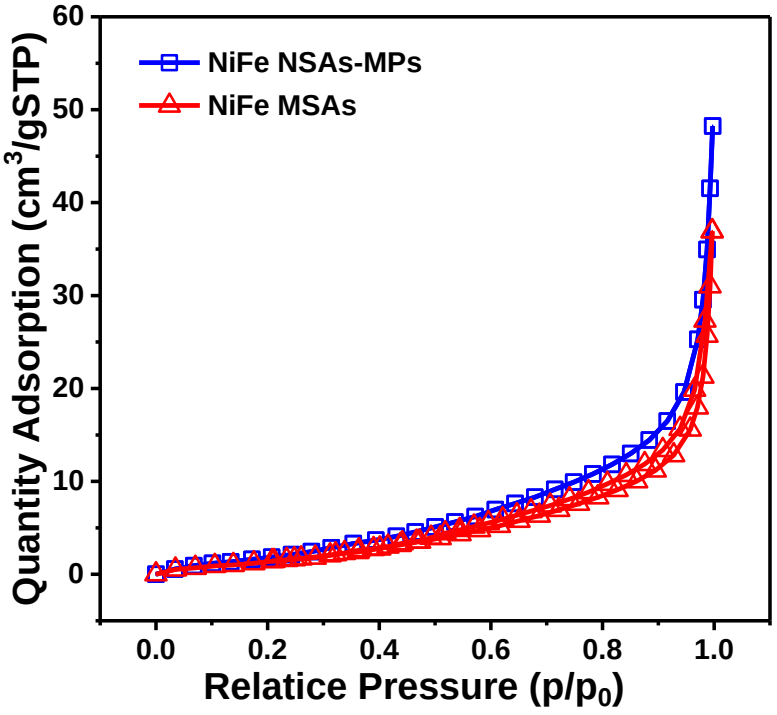

Figure S18. N_2 adsorption-desorption isotherms of NiFe NSAs-MPs and NiFe MSAs at 70℃.

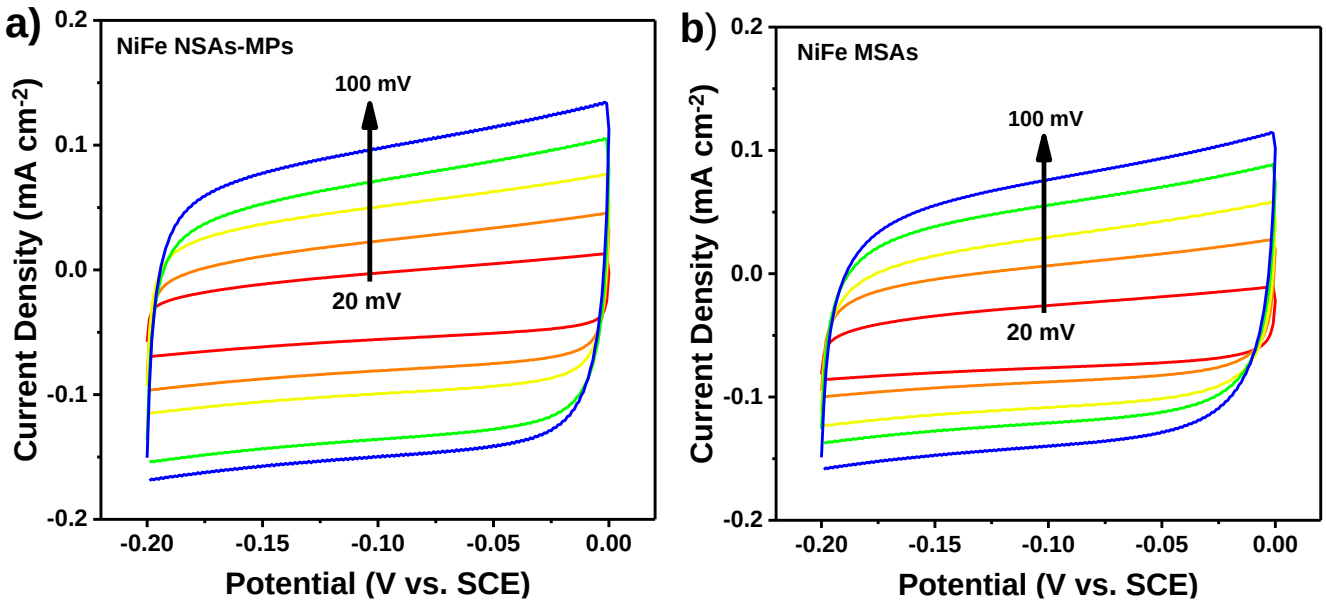

Figure S19. CVs of (a) NiFe NSAs-MPs and (b) NiFe MSAs at the different scan rates from 20 to 100 mV s^{-1} in the potential range of -0.2~0 V (*vs* SCE).

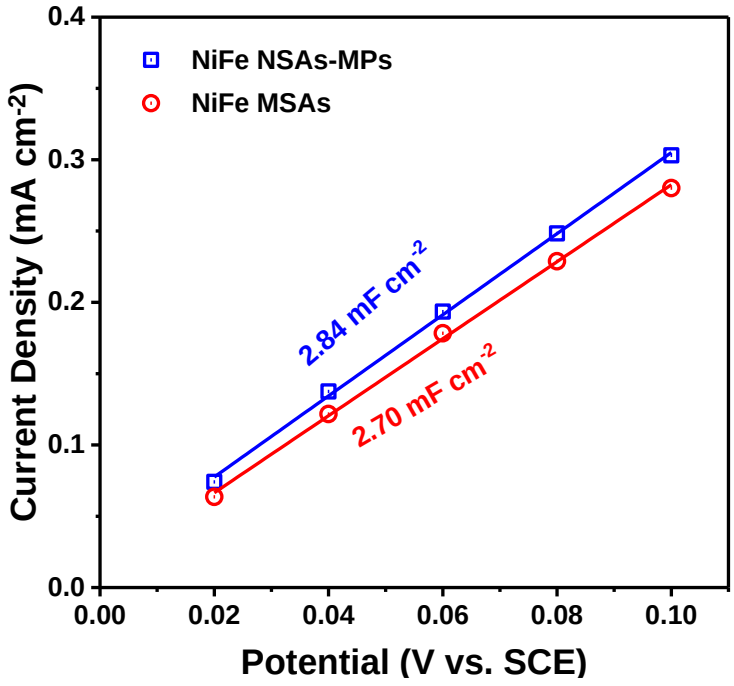

Figure S20. Capacitive current density at 0.1 V (*vs* SCE) as a function of scan rate for NiFe NSAs-MPs and NiFe MSAs.

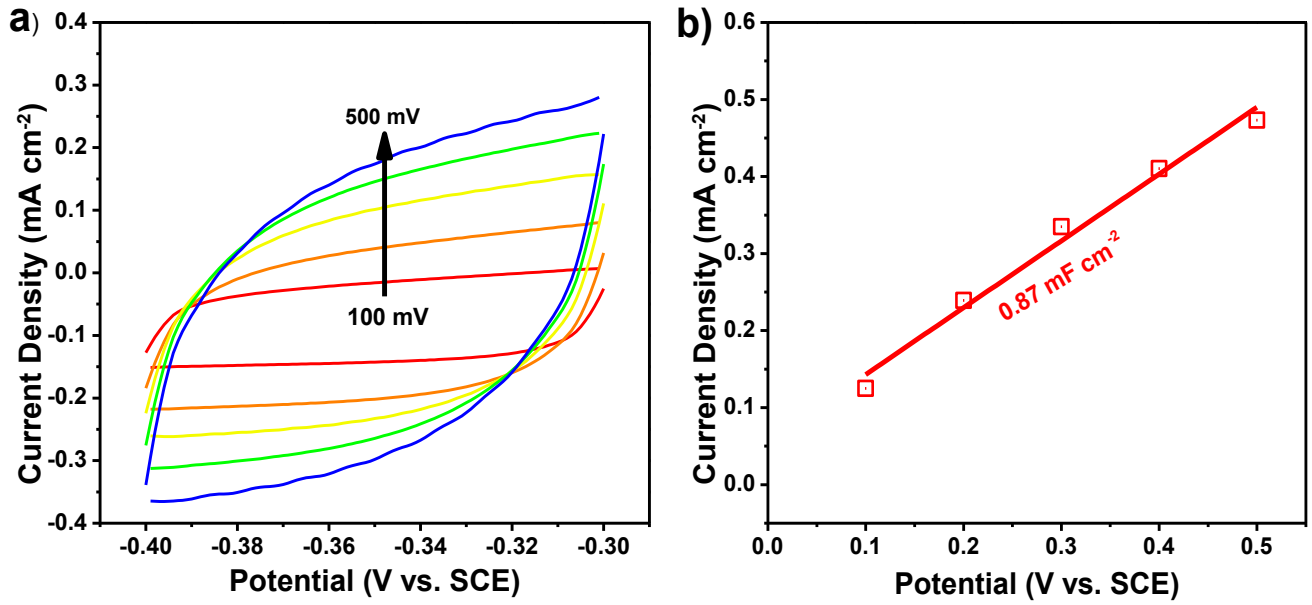

Figure S21. (a) CVs of NF at the different scan rates from 100 to 500 mV s^{-1} in the potential range of -0.4 ~ -0.3 V (*vs* SCE); (b) Capacitive current density at -0.35 V (*vs* SCE) as a function of scan rate for NF.

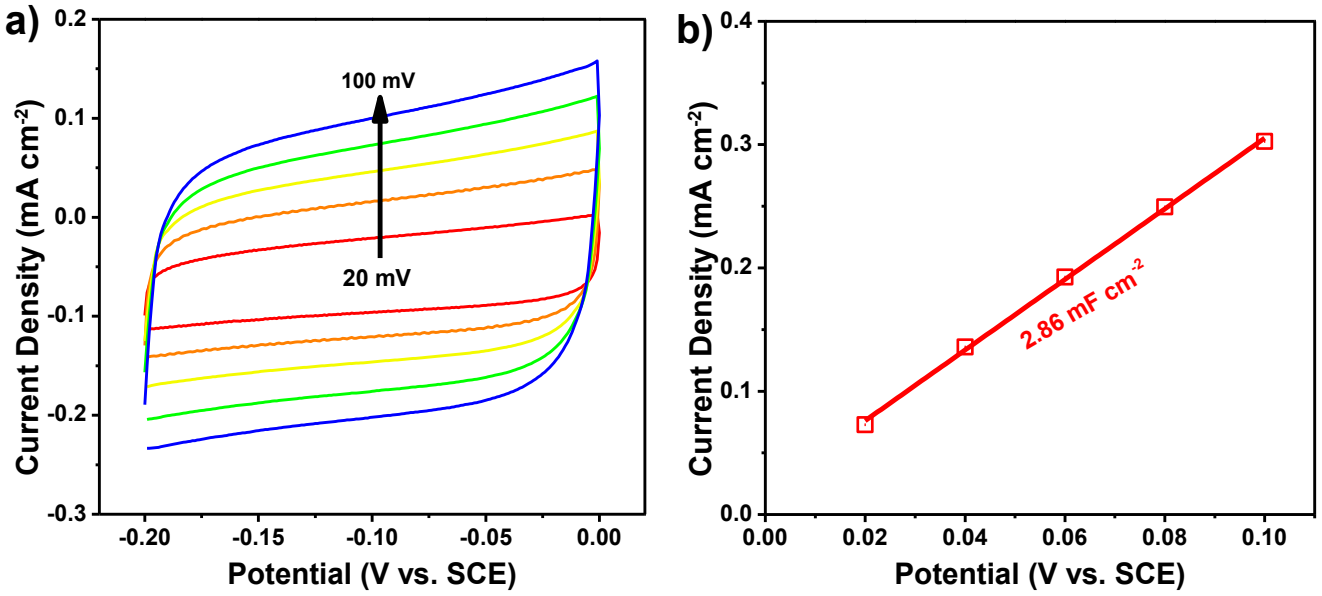

Figure S22. (a) CVs of hydrated NF at the different scan rates from 20 to 100 mV s^{-1} in the potential range of -0.2 ~ 0 V (*vs* SCE); (b) Capacitive current density at 0.1 V (*vs* SCE) as a function of scan rate for the hydrated NF.

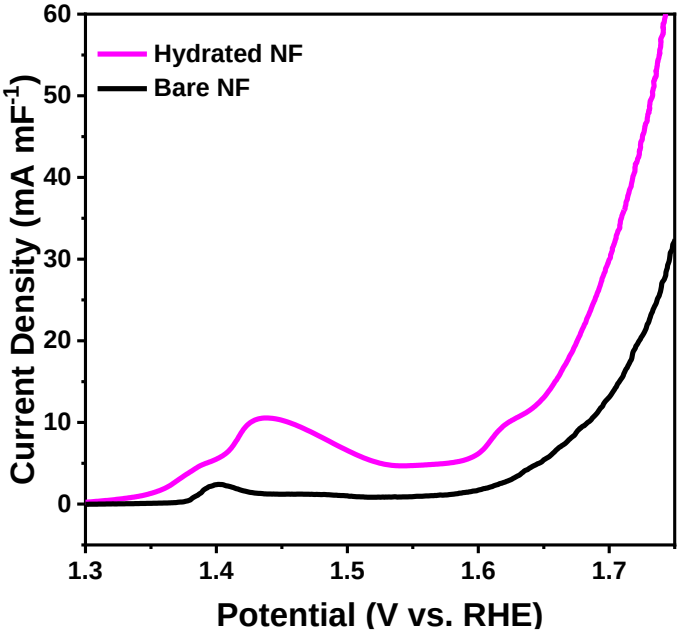

Figure S23. LSVs of the hydrated NF and bare NF normalized by ECSA.

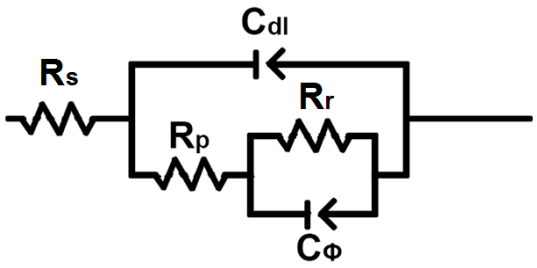

Figure S24. The Armstrong-Henderson (A-H) model.

The Armstrong-Henderson (A-H) model offered the best fit for hydroxides films. The polarisation resistance R_p represents the total charge transfer resistance and the C_Φ-R_r loop models with the relaxation of charge associated with a surface concentration (C_Φ is the value of capacitance, and R_r represents the resistance of the relaxing of charge).

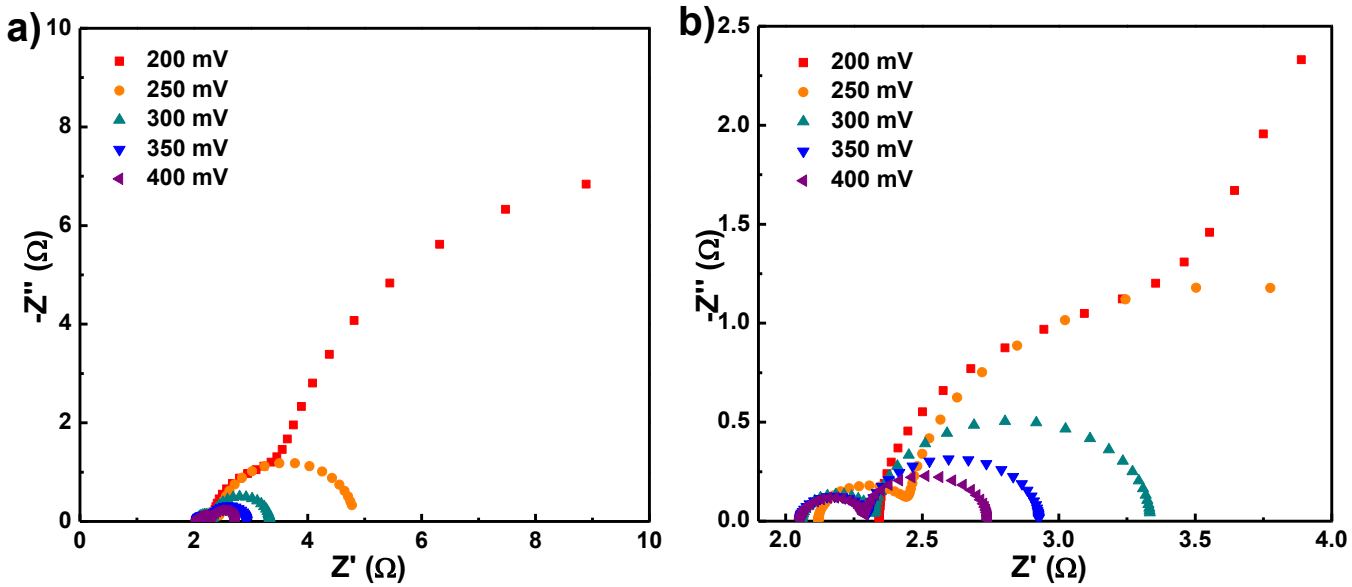

Figure S25. (a) EIS and (b) the zoom-in EIS pattern of NiFe NSAs-MPs at sequential overpotential from 200 to 400 mV.

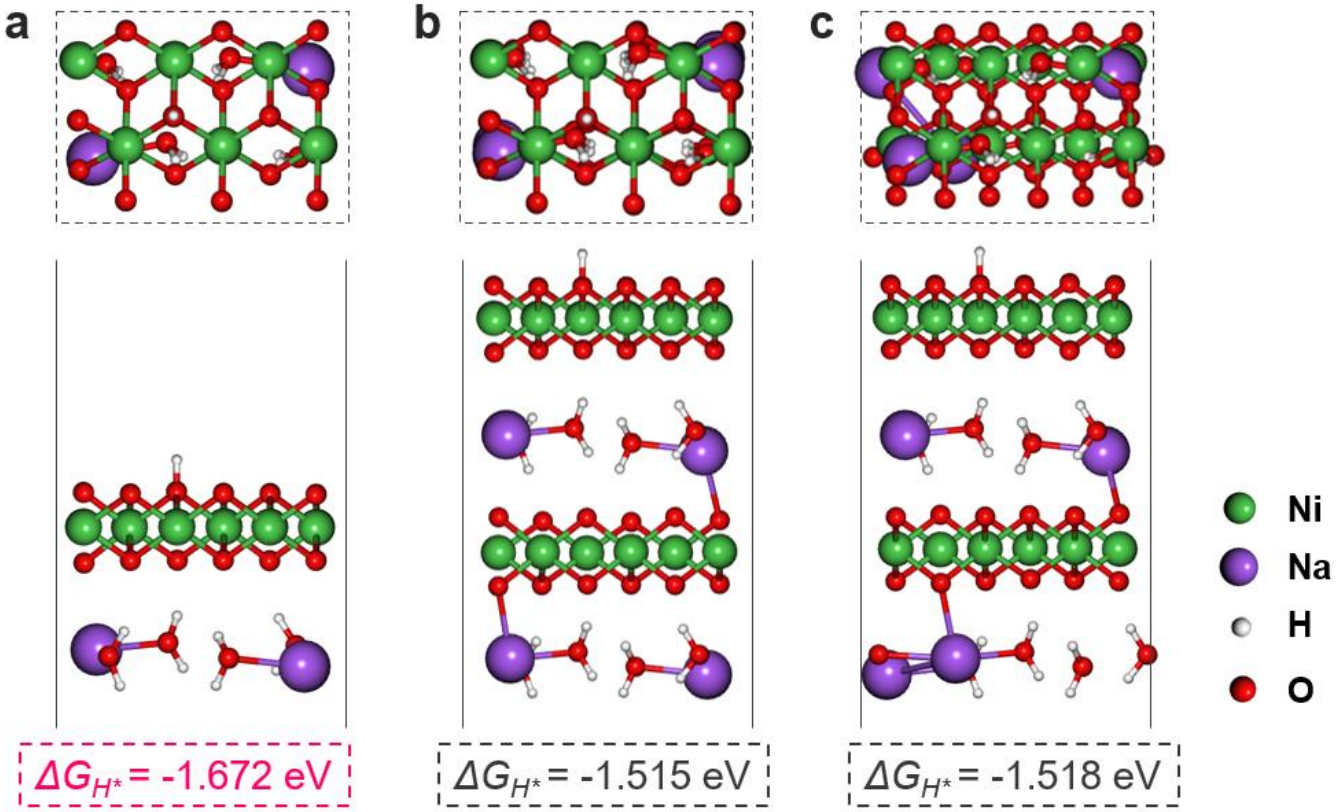

Figure S26. H^* adsorption energy of single layer (a), double layer (b) and double layer with lattice dislocation (c) of γ-NiOOH.

To obtain the direct evidence of the influence of adsorption energy, the simplest and universally applicable H^* adsorption energy changes were made in three different cases. It can be seen that the adsorption energies of single layer (a) and double layer (b) are considerably different (~10%), and the lattice dislocation of upper and lower layers (c) has little effect on the adsorption energies (<1%), so the calculation of adsorption energies by single layer modeling is reasonable.

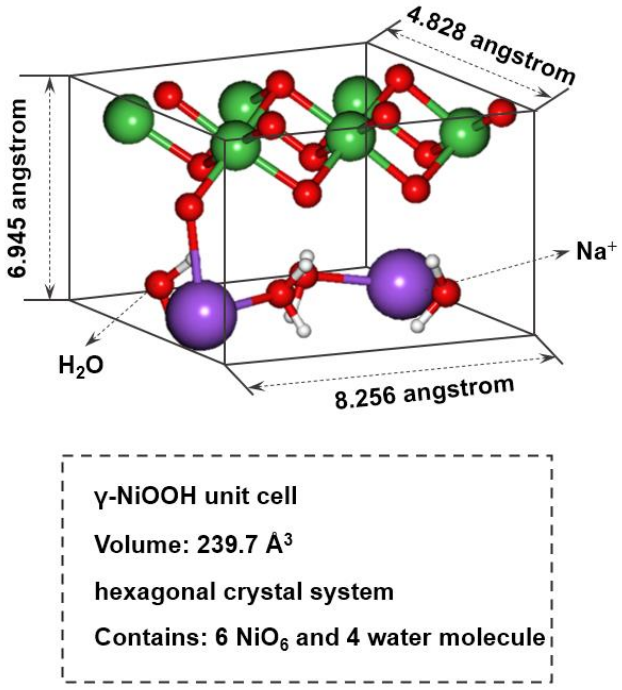

Figure S27. Model and crystal information of γ-NiOOH.

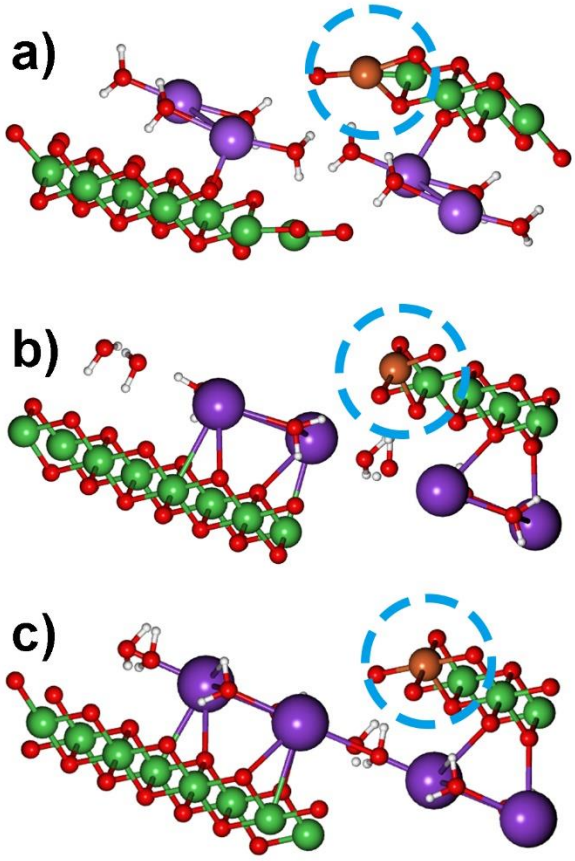

Figure S28. The (012) plane of NiFe LDHs in which the Fe atom is coordinated with three, four and five oxygen atoms.

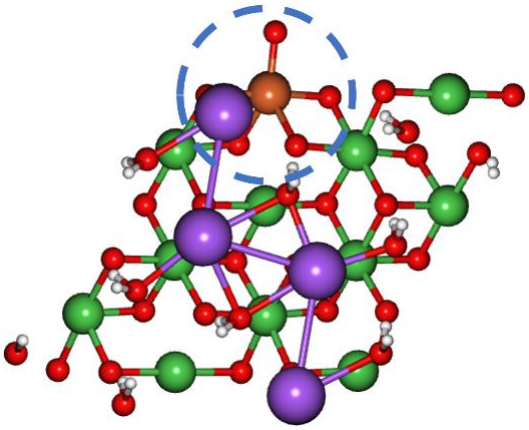

Figure S29. The O* intermediate on (110) plane of NiFe LDHs, and it shows an unstable geometric structure of Fe coordinated with five oxygen atoms.

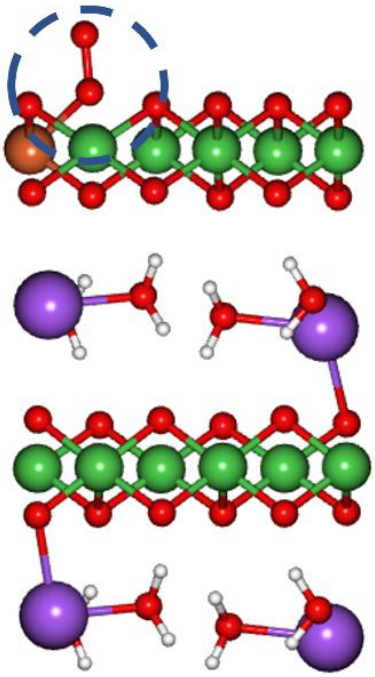

Figure S30. The O* intermediate on (003) facet of NiFe LDHs. The adsorbed O atom is located at the bridge site since all Ni and Fe atoms are already full-coordinated, thus the O* intermediate makes it difficult to connect a second OH^- to form HOO*.

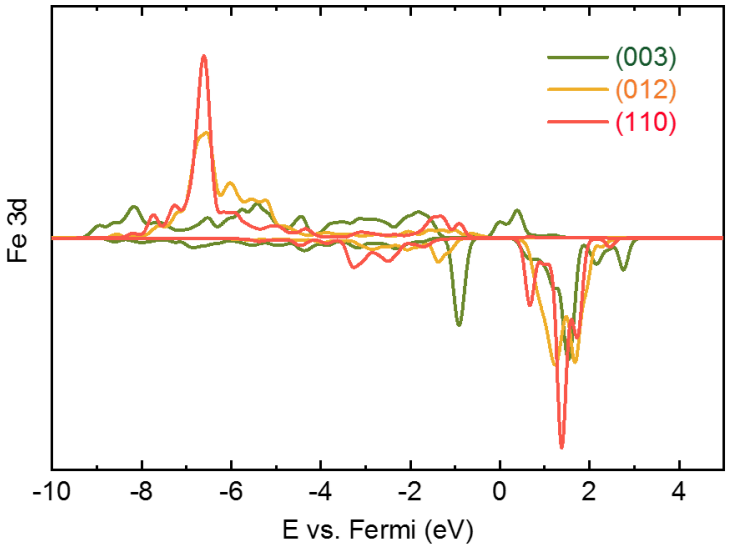

Figure S31. The full range DOS in Figure 6a of (003), (012) and (110) planes of NiFe LDHs.

To reveal the real active phase of the NiFe catalyst, we have characterized the NiFe NSAs-MPs by *in-situ* Raman spectra. Figure S32 shows the experimental set-up for the *in-situ* Raman spectra study. The objective was wrapped in a PE film to prevent direct contact between the lens and electrolyte. The counter electrode, reference electrode, and working electrode are carbon rod, saturated calomel electrode, and NiFe NSAs-MPs, respectively. Laser excitation was conducted at 532 nm at a grating of 1800 l/mm.

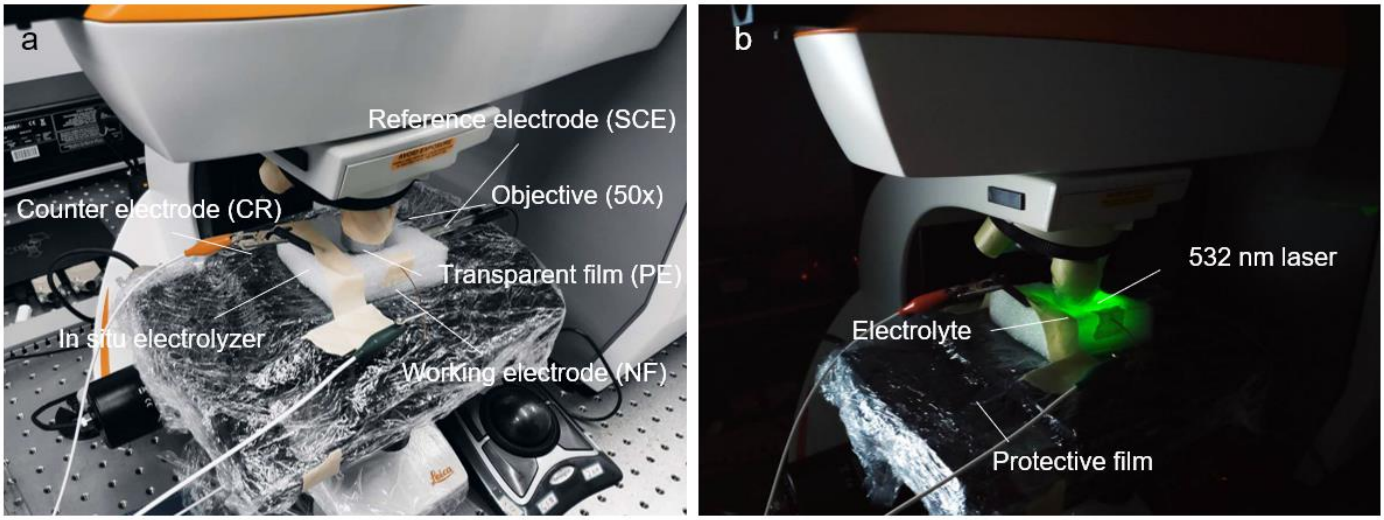

Figure S32. *In-situ* Raman spectra test image before (a) and during the OER (b).

The different laser power tests were conducted, and the results show a signal of 1% power is the best, as shown in Figure S33. Higher laser power may lead to an irreversible change in materials. And we find that the PE film peak will occur when laser power higher than 5%.

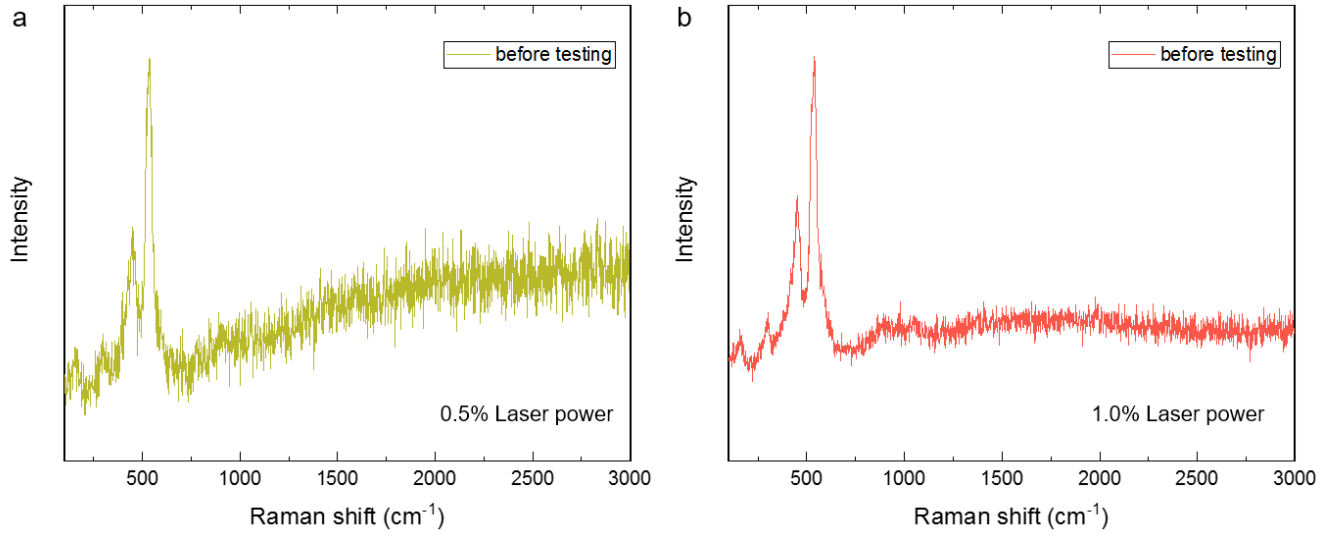

Figure S33. Raman spectra of NiFe NSAs-MPs with 0.5% laser power (a) and 1.0% laser power (b).

During the test, we found that under the potential of 1.53 V vs. RHE, significant OER occurs on the surface of the catalyst, accompanied by a large number of bubbles, as shown in Figure S34.

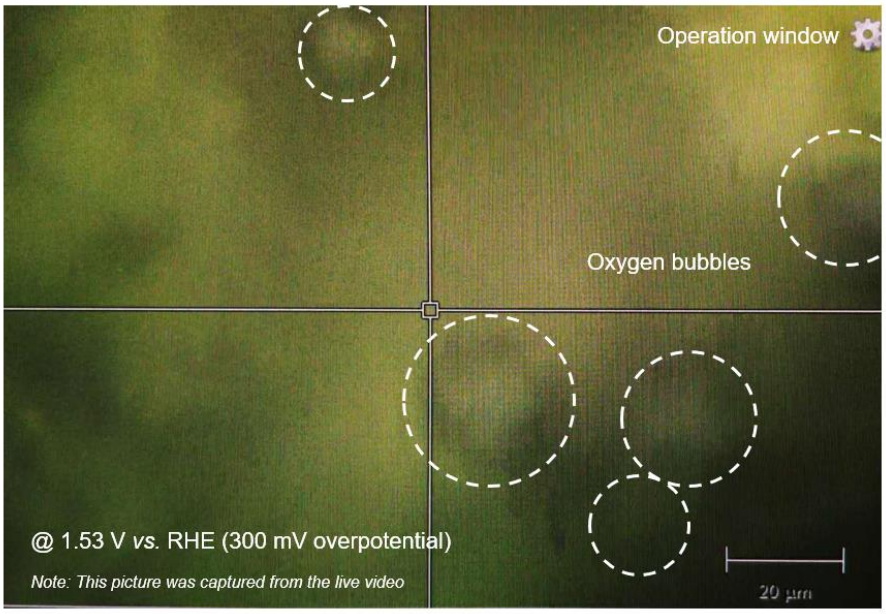

Figure S34. The operation window of Raman spectra during OER (@1.53 V vs. RHE).

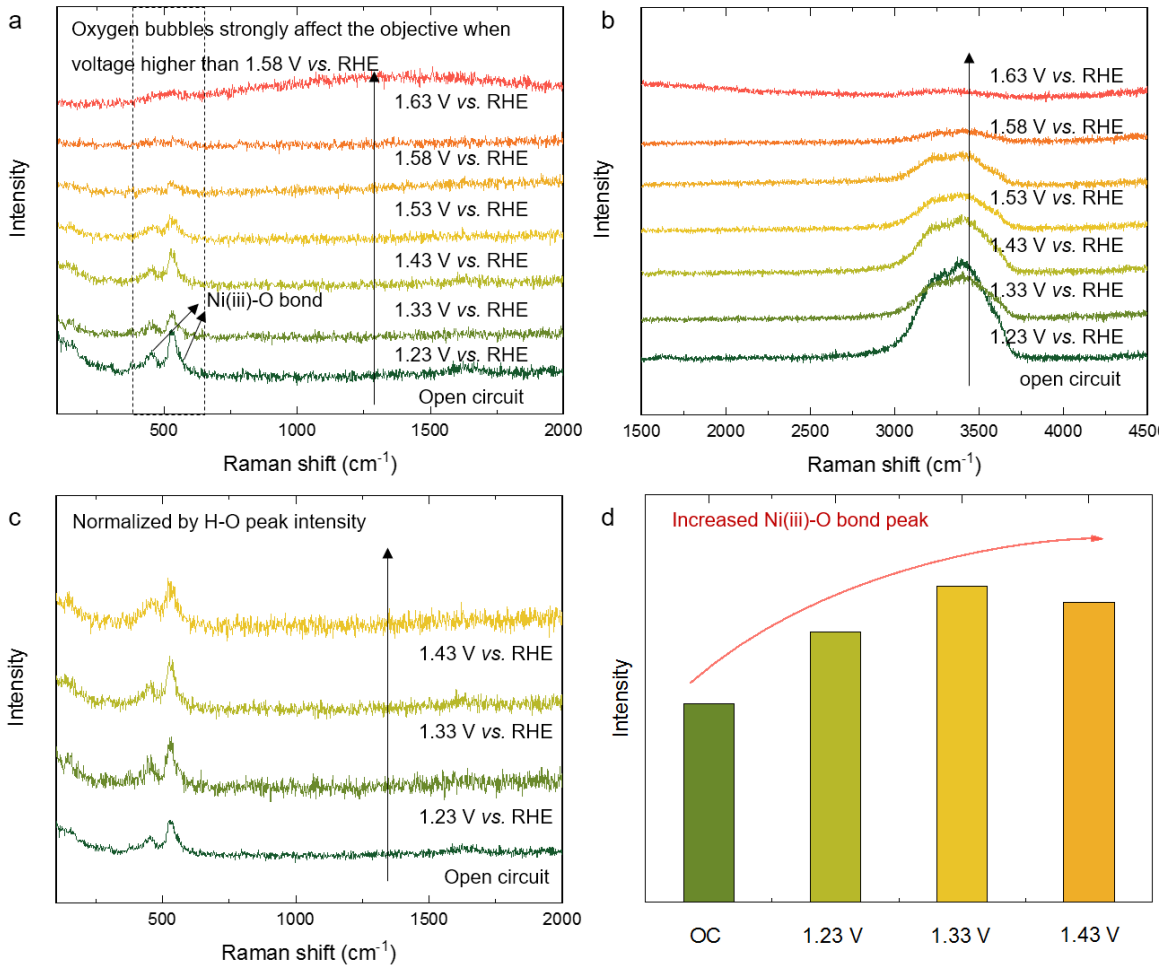

Figure S35. In situ Raman spectra collected at (a) low and (b) high wavenumbers for NiFe NSAs-MPs as a function of potential vs. RHE in 1 M KOH. (c) In situ Raman spectra normalized by H-O peak intensity and the (d) Ni-O peak intensity under different voltage.

Figure S35 shows a series of Raman spectra for NiFe NSAs-MPs and immersed in 1 M KOH, acquired as a function of the applied potential (vs. RHE) during an oxidation sweep. The two peaks around 500 cm^{-1} are attributed to the $\delta(Ni^{iii}\text{-}O)$ and $\nu(Ni^{iii}\text{-}O)$.[22] The two peaks also occurred during the open circuit, which is caused by the aging process.[23] We found that the catalyst reacts violently at high potential (higher than 1.58 V vs. RHE), and the objective lens is hard to focus, which makes it difficult to capture the high-intensity signal, as shown in Figure S35a and S35b. To compare the intensity of the two peaks during different potential, we normalize the peaks by the intensity of O-H in H_2O molecules, as shown in Figure S34. We find that the Ni-O peak intensity was increased after 1.23V vs. RHE, which indicates that the surface deprotonation step occurs before OER, consisted with previous studies.[24] This result also proves that the real active structure is $Na_{⅓}(H_2O)_{⅔}(Ni,Fe)O_2$, consisted with our DFT calculations.

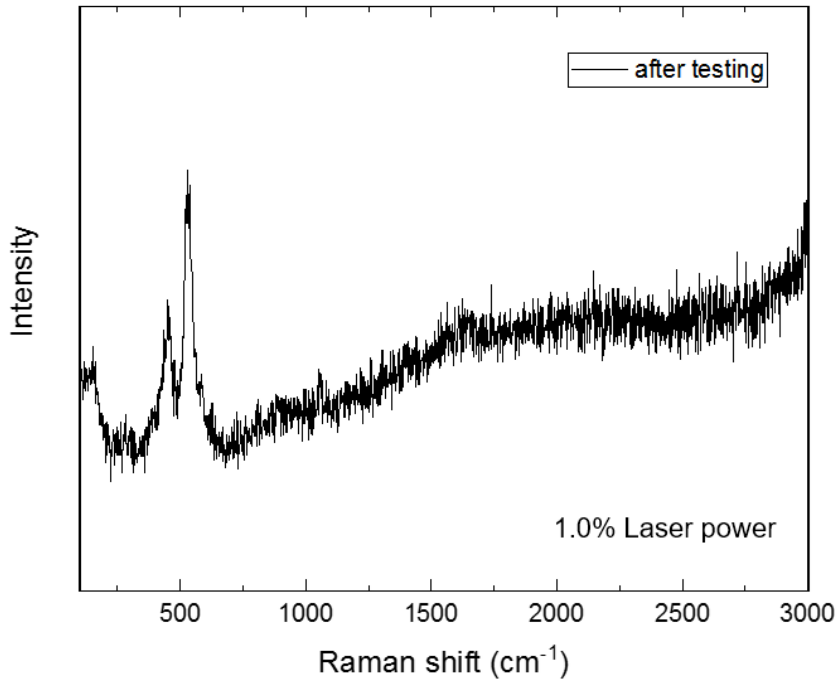

Figure S36. In situ Raman spectrum collected at low wavenumbers for NiFe NSAs-MPs.

The Raman spectrum of NiFe NSAs-MPs was characterized after OER as shown in Figure S36, and there was no change or additional peaks, indicating the stability of the whole structure. The intensity of $\delta(Ni^{iii}\text{-}O)$ and $\nu(Ni^{iii}\text{-}O)$ still exists, also indicating that the active phase is the dehydrogenated NiFe LDHs.

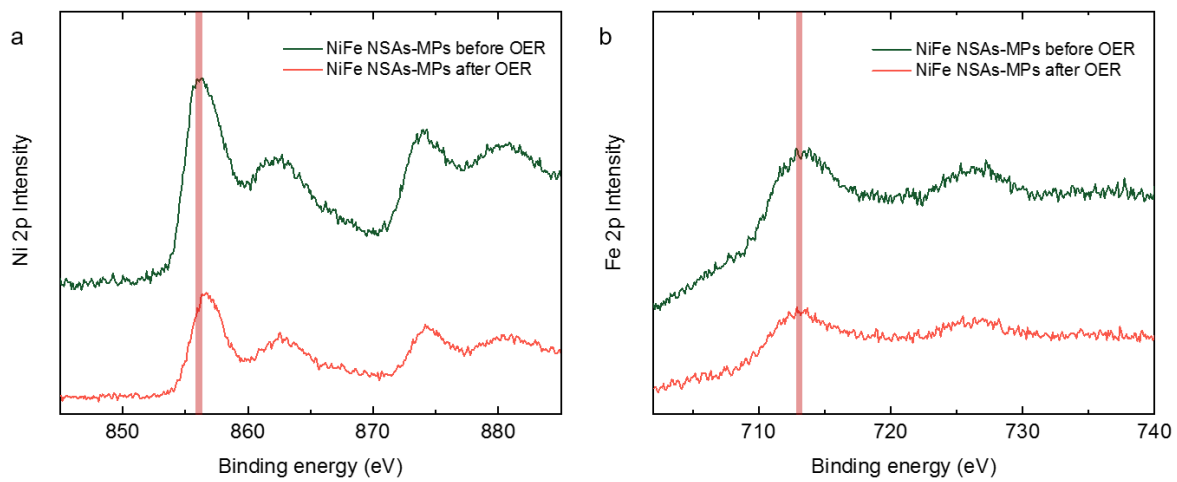

Figure S37. The comparisons of Ni 2p (a) and Fe 2p (b) XPS spectra of NiFe NSAs-MPs before and after OER.

The XPS spectra of NiFe NSAs-MPs were characterized to find out the valence changes before and after OER as shown in Figure S37. The Ni $2p_{3/2}$ peak was shifted from 856.2 eV to 856.7 eV, consistent with the formation of dehydrogenated NiFe LDHs.[25]

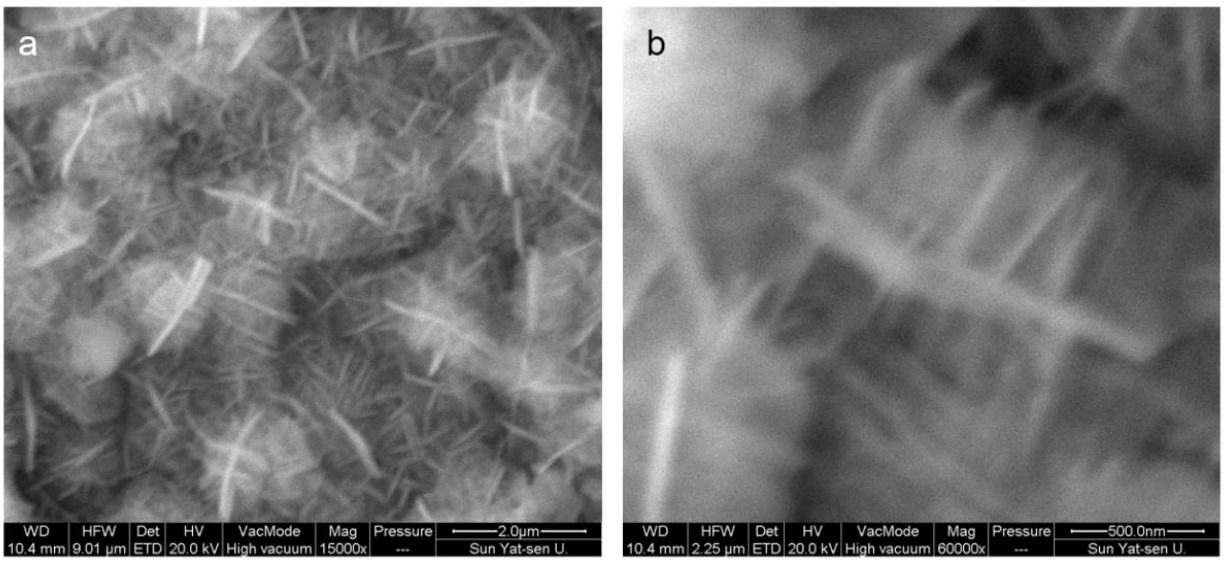

Figure S38. (a,b) SEM images of NiFe NSAs-MPs after OER with different magnifications.

SEM images were utilized to judge the surface morphology stability of NiFe NSAs-MPs after 40 h chronopotentiometric test at 100 mA cm^{-2}, as shown in Figure S38, which shows that the morphology of NiFe NSAs-MPs is hardly changed after OER.

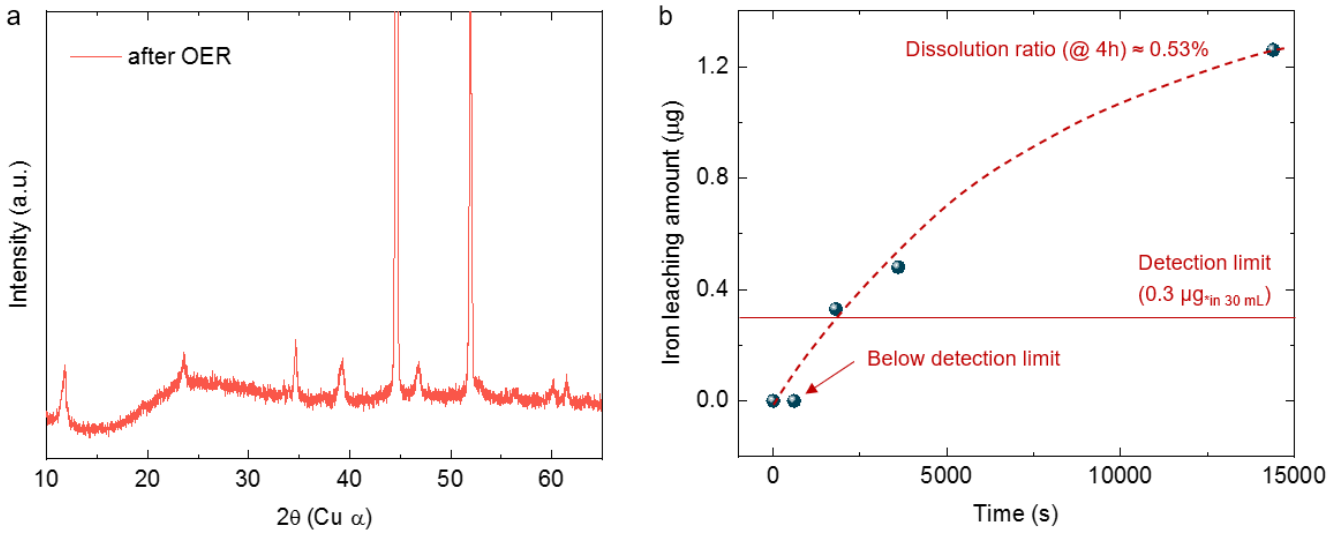

Figure S39. (a) XRD patterns of NiFe NSAs-MPs after the OER; (b) The drop rate of the catalyst during the OER process.

To further confirm the structure stability of NiFe NSAs-MPs, we also performed XRD after 40 h OER as shown in Figure S39a. The result indicates that the NiFe NSAs-MPs is still crystalline. The slightly reduced intensity can be attributed to the drop of catalyst, which is further confirmed by ICP-AES, as shown in Figure S39b. The drop mass of the catalyst is ~0.5% for 4-hours test and the drop rate decreases with time. The performance of the NiFe NSAs-MPs is hardly changed during chronopotentiometric test, indicating that the dropped catalyt is the outer layer.

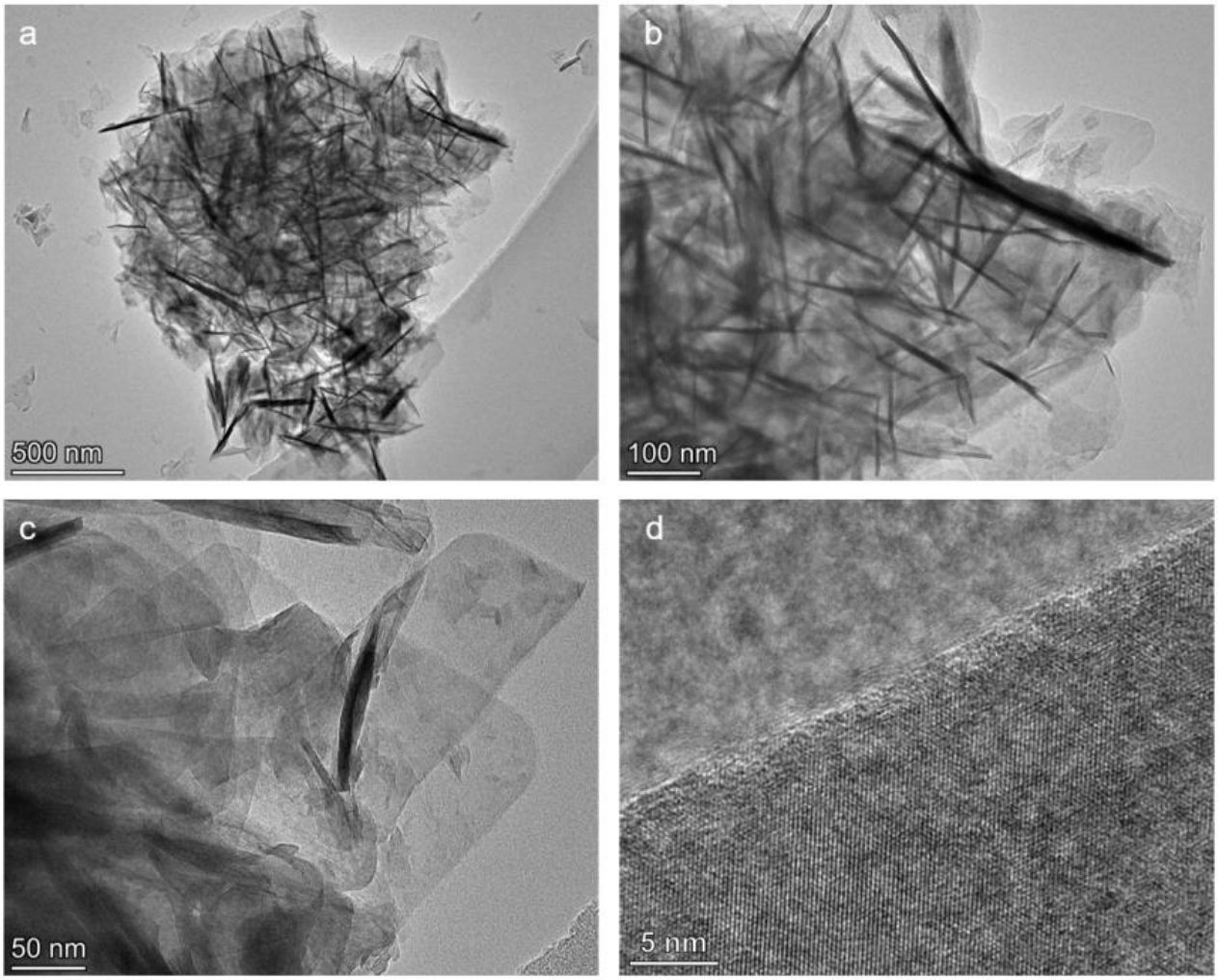

Figure S40. (a-c) TEM and (d) HRTEM images of NiFe NSAs-MPs after the OER.

Finally, we performed the TEM characterizations to confirm the structural stability of NiFe NSAs-MPs after OER. Figure S40a-c clearly shows the hierarchal NiFe LDHs nanosheet-arrays-on-microplates. The surface of microplates is still crystalline (Figure S40d), consisted with the XRD result, which also indicates that the surface of NiFe NSAs-MPs is stable.

Table S1. The plane information from the XRD pattern of PDF cards of nickel iron hydroxide carbonate hydrates (CO_3^{2-} intercalated NiFe LDHs). The previous PDF cards of NiFe LDHs also show that the peak of (003) facet is far stronger than the edge planes.[10]

PDF#40-0215		PDF#49-0188		PDF#51-0463	
Plane	I% (Height)	Plane	I% (Height)	Plane	I% (Height)
(003)	100.0	(003)	100.0	(003)	100.0
(006)	55.0	(006)	37.0	(006)	37.0
(101)	25.0	(101)	8.0	-	-
(012)	40.0	(012)	40.0	(012)	27.0
(015)	15.0	(015)	12.0	(015)	12.0
(018)	6.0	(018)	10.0	(018)	8.0
(110)	30.0	(110)	20.0	(110)	17.0
(113)	35.0	(113)	18.0	(113)	16.0

Table S2.1 The plane information from XRD pattern of NiFe NSAs-MPs.

2-Theta	d(A)	Facet	I% (Height)
11.920	7.4183	(003)	77.3
23.860	3.7263	(006)	34.8
34.620	2.5888	(012)	100.0
39.320	2.2895	(015)	54.8
46.960	1.9333	(018)	48.3
60.060	1.5392	(110)	36.6
61.400	1.5087	(113)	33.7

Table S2.2 The plane information from XRD pattern of NiFe MSAs.

2-Theta	d(A)	Plane	I% (Height)
11.660	7.5833	(003)	100.0
23.519	3.7796	(006)	21.3
34.470	2.5997	(012)	56.5
39.050	2.3047	(015)	31.4
46.720	1.9427	(018)	16.5
59.900	1.5429	(110)	26.3
61.200	1.5132	(113)	24.4

Table S3.1 Optimum fitting parameters for EIS patterns of NiFe NSAs-MPs.

Overpotential (mV)	R_s/Ω	C_{dl}/mF cm^{-2}	R_p/Ω	$R_r/\ \Omega$	C_Φ/mF cm^{-2}
200	2.343	0.03275	2.063	13.21	0.1208
250	2.12	0.003231	0.3577	2.345	0.09256
300	2.058	0.000398	0.2711	1.007	0.06611
350	2.052	0.000311	0.2507	0.6247	0.0533
400	2.053	0.000244	0.237	0.4513	0.044477

Table S3.2 Optimum fitting parameters for EIS patterns of NiFe MSAs.

Overpotential (mV)	R_s/Ω	C_{dl}/mF cm^{-2}	R_p/Ω	$R_r/\ \Omega$	C_Φ/mF cm^{-2}
200	2.883	0.05404	1.188	9.233	0.195
250	2.817	0.02401	0.4467	1.891	0.1865
300	2.746	0.0009549	0.3186	0.9384	0.01241
350	2.707	0.0001089	0.2646	0.6321	0.09922
400	2.707	0.0001148	0.2646	0.5068	0.0877

Table S4. Comparisons of the activities of NiFe LDH-based electrocatalysts for OER.

Catalysts	**Electrolyte**	**Current Density /mA cm^{-2}**	**Overpotential /mV**	**Tafel/mV dec^{-1}**	**References**
NiFe NSAs-MPs	1.0 M KOH	10 100	210 250	34.5	This work
NiFe MSAs	1.0 M KOH	10 100	210 300	63	This work
hydrated NF	1.0 M KOH	10 100	145 470	140	This work
NF	1.0 M KOH	10 100	460 615	137.4	This work
NiFe LDH/CNT	0.1M KOH 1.0 M KOH	10 10	308 257	31	[11]
NiFe LDH/rGO	1.0 M KOH	10	210	42	[12]
NiFe LDH/DG	1.0 M KOH	20	270	52	[13]
Exfoliated NiFe LDH	1.0 M KOH	10	300	40	[14]
NiFe LDH/NF	1.0 M KOH	10 100	224 380	52.8	[15]
NiFe LDH h-MS	1.0 M KOH	10 71.7	239 300	53	[16]
FeOOH/NiFe LDH	1.0 M KOH	10 500	208 288	42	[17]
NiFe LDH h-NP	1.0 M KOH	10	280	49.4	[18]
NiFe LDH/Cu NW	1.0 M KOH	10 100	199 281	27.8	[19]
Ultrafine NiFe LDH	1.0 M KOH	10	254	32	[20]
NiFe LDH/sa-Au	1.0 M KOH	10	237	36	[21]

Table S5. Coordinates for the initial cell of γ-NiOOH, which is a modified model proposed by Ceder and Goddard.

γ-NiOOH			
H	0.794299	0.788244	0.345545
H	0.742433	0.776806	0.127096
H	0.749836	0.443840	0.139585
H	0.775596	0.425085	0.357834
H	0.317656	0.235451	0.291315
H	0.247679	0.218187	0.063709
H	0.236351	0.561154	0.063599
H	0.304290	0.571633	0.269430
O	0.756582	0.847938	0.231339
O	0.670903	0.390960	0.245803
O	0.205278	0.178824	0.188203
O	0.169660	0.607789	0.178222
O	0.573158	0.750462	0.856203
O	1.044704	0.256510	0.840112
O	0.857626	0.747961	0.557942
O	0.390917	0.250724	0.561085
O	0.854603	0.085766	0.555533
O	0.391711	0.581762	0.559464
O	0.574839	0.090077	0.859221
O	1.044462	0.583884	0.834315
O	0.883714	0.417803	0.564426
O	0.545231	0.420141	0.845795
O	0.390124	0.915437	0.561901
O	1.043315	0.919433	0.840218
Na	0.765339	0.136332	0.217652
Na	0.237715	0.876796	0.142100
Ni	0.713371	0.584930	0.703599
Ni	0.714777	0.251479	0.704826
Ni	0.216216	0.086501	0.700991
Ni	0.217539	0.750881	0.697721
Ni	0.218389	0.418590	0.697468
Ni	0.714051	0.917265	0.704280

Table S6. Coordinates for the (003) plane of ($Na_{⅓}(H_2O)_{⅔}(Ni,Fe)O_2$).

O	2.867822000	5.977431000	15.548775000
O	2.887850000	0.505295000	15.548352000
O	2.738448000	3.241323000	15.465650000
O	0.306427000	7.380165000	15.437419000
O	0.324965000	1.887289000	15.415097000
O	0.317709000	4.600398000	15.385261000
Ni	3.538766000	7.373874000	14.491552000
Fe	3.541386000	4.620256000	14.475998000
Ni	3.554179000	1.857214000	14.473705000
Fe	1.149827000	0.489319000	14.447074000
Ni	1.144218000	5.994585000	14.445833000
Ni	1.154242000	3.241288000	14.433244000
O	1.968886000	7.371011000	13.500658000
O	4.361012000	3.248704000	13.496639000
O	1.984549000	1.863361000	13.473329000
O	1.982405000	4.606453000	13.472762000
O	4.228891000	5.984881000	13.462381000
O	4.226017000	0.498229000	13.424049000
H	3.830259000	3.327776000	12.055156000
H	3.913562000	6.338042000	11.980929000
H	1.619856000	1.761455000	11.589469000
H	1.548412000	4.548994000	11.447695000
O	3.320719000	3.055066000	11.272743000
O	3.725632000	6.843077000	11.185629000
Na	3.780045000	0.948086000	11.066791000
O	1.073992000	1.301456000	10.868700000
O	0.893946000	4.856629000	10.813337000
Na	1.216221000	7.089081000	10.569044000
H	3.696449000	3.503196000	10.531717000
H	3.654240000	6.263244000	10.455402000
H	1.211997000	4.480934000	10.010512000
H	1.272816000	1.639172000	10.000000000

Table S7. Coordinates for the (110) plane of ($Na_{⅓}(H_2O)_{⅔}(Ni,Fe)O_2$).

O	3.776184000	-6.429332000	18.107068000
Ni	4.694587000	-8.001302000	18.047065000
Fe	4.825948000	-3.216816000	18.034381000
O	5.662790000	-4.775583000	18.118191000
O	5.603085000	-9.571816000	18.090881000
O	3.869255000	-1.708475000	18.090461000
Na	1.447490000	-2.142935000	17.653609000
H	1.748435000	-6.384553000	17.553997000
H	0.309921000	-6.469097000	17.227147000
O	1.103569000	-6.969222000	17.144505000
O	5.981386000	-2.354392000	16.824275000
O	3.627542000	-4.038350000	16.728003000
Ni	4.668555000	-5.623889000	16.690185000
Ni	4.882021000	-0.820613000	16.688351000
O	5.667551000	-7.172013000	16.570539000
O	3.726630000	-8.821612000	16.559318000
O	1.606446000	-0.126044000	16.430269000
H	2.230794000	-9.184078000	16.337774000
H	1.938468000	-3.948034000	16.203871000
H	0.885688000	0.351450000	16.073840000
H	0.348536000	-3.988337000	15.840151000
O	1.221231000	-3.814324000	15.499055000
O	5.846001000	-0.073158000	15.233656000
O	3.865939000	-1.614149000	15.229718000
O	3.788860000	-6.404919000	15.232232000
Ni	4.743670000	-3.229065000	15.203965000
O	5.668276000	-4.829644000	15.257107000
Ni	4.717913000	-8.018912000	15.208378000
H	2.355838000	-6.632652000	14.741296000
H	0.828575000	-6.822847000	14.712328000
Na	0.965215000	-1.597374000	14.390210000
O	1.574058000	-6.640833000	14.162566000
O	3.904571000	0.767576000	13.811541000
Ni	4.845346000	-0.850059000	13.786690000
Ni	4.767561000	-5.620961000	13.775371000
O	5.704684000	-7.246288000	13.812292000
O	5.825536000	-2.447562000	13.746174000
O	3.793178000	-4.041058000	13.644668000
Na	1.407959000	-4.587975000	13.491043000
H	1.889893000	0.743957000	13.391431000
H	0.451379000	0.659413000	13.064581000
O	1.245027000	0.159288000	12.981939000
O	5.862693000	-4.844632000	12.461076000
O	3.747496000	-6.418012000	12.428795000
Ni	4.886946000	1.544939000	12.380412000
Ni	4.884047000	-3.253033000	12.327879000
O	5.842300000	-0.032460000	12.462368000

O	3.911420000	-1.650508000	12.369957000
O	1.566915000	-2.571083000	12.267703000
H	2.372253000	-2.055569000	12.175208000
H	1.898937000	-6.393074000	12.041305000
H	0.846157000	-2.093589000	11.911274000
H	0.309005000	-6.433377000	11.677584000
O	1.181700000	-6.259363000	11.336489000
O	5.874567000	-2.595323000	10.851456000
O	4.025602000	-3.921449000	10.804645000
O	4.137090000	0.834363000	10.849449000
Ni	4.771262000	-5.663074000	10.879016000
O	5.787450000	2.210964000	10.902049000
Ni	5.002795000	-0.868838000	10.847259000
H	2.497296000	0.495858000	10.578729000
H	0.970033000	0.305663000	10.549762000
Na	0.925683000	-4.042414000	10.227644000
O	1.715517000	0.487676000	10.000000000

Table S8. Coordinates for the (012) plane of ($Na_{⅓}(H_2O)_{⅔}(Ni,Fe)O_2$).

O	0.969308000	7.719658000	9.858409000
O	0.311362000	10.760590000	16.086811000
O	3.222251000	20.982645000	15.985384000
O	4.251824000	17.484966000	9.553926000
Fe	0.935773000	12.523159000	15.686064000
H	1.521388000	19.666888000	15.779156000
O	2.720243000	9.381420000	15.519061000
H	3.597982000	21.681720000	15.474275000
O	1.479901000	14.215909000	15.599943000
H	3.585292000	20.965451000	16.960384000
Ni	3.473453000	11.107850000	15.261294000
O	0.306260000	8.116462000	14.980936000
Na	3.681577000	19.117750000	14.983412000
O	0.975524000	19.520164000	14.936792000
O	3.958429000	12.874587000	15.320923000
Ni	1.096485000	9.794232000	14.636696000
H	3.837491000	16.120754000	14.722508000
O	2.625164000	24.794073000	14.434662000
O	1.892759000	11.490155000	14.323284000
H	1.174348000	20.166552000	14.265321000
Ni	3.505609000	8.475248000	14.092745000
O	3.649560000	16.893254000	14.183243000
O	0.096351000	23.319127000	13.895813000
O	4.350286000	10.093909000	13.675480000
Na	1.140150000	17.357860000	13.709075000
Ni	1.083627000	7.137766000	13.551437000
H	3.754187000	13.314365000	13.630995000
O	2.583679000	22.128218000	13.365480000
H	1.472341000	14.675354000	13.541044000
O	1.937258000	8.962050000	13.185997000
H	3.578168000	16.639595000	13.285972000
Ni	3.376983000	23.809592000	12.997433000
O	0.817875000	15.203681000	13.074225000
O	0.200989000	20.825711000	12.842464000
O	3.244647000	13.364220000	12.803917000
O	4.250779000	7.461746000	12.642274000
Ni	0.966364000	22.497945000	12.456460000
H	1.543784000	12.048465000	12.597690000
O	2.618284000	19.496319000	12.370963000
H	3.620378000	14.063295000	12.292808000
O	1.857204000	6.152874000	12.082946000
H	1.135925000	15.166371000	12.188628000
Ni	3.404186000	21.167473000	11.940548000
O	0.190394000	18.253631000	11.910638000
Na	3.703974000	11.499326000	11.801946000
O	0.997920000	11.901739000	11.755325000
O	4.177951000	22.843415000	11.557733000

Ni	1.012496000	19.849454000	11.425417000
H	3.859887000	8.502330000	11.541041000
O	2.691863000	16.829168000	11.367440000
O	1.817334000	21.529045000	11.035982000
H	1.196744000	12.548127000	11.083854000
Ni	3.453726000	18.494097000	10.933877000
O	3.671957000	9.274829000	11.001777000
O	0.670902000	15.386899000	10.344754000
O	4.227087000	20.198431000	10.535787000
Na	1.162546000	9.739436000	10.527608000
Ni	1.095469000	17.156718000	10.377478000
H	1.679183000	7.524764000	9.285304000
O	3.055707000	13.908303000	10.039908000
H	1.494737000	7.056930000	10.359578000
O	1.837810000	18.886418000	10.049571000
H	3.600564000	9.021170000	10.104506000
Ni	3.638232000	15.639607000	9.986235000

References

1. H. Shin, H. Xiao, W. A. Goddard and III, *J. Am. Chem. Soc.*, 2018, **140**, 6745-6748.
2. Kostecki and Robert, *J. Electrochem. Soc.*, 1997, **144**, 485.
3. D. S. Hall, D. J. Lockwood, S. Poirier, C. Bock and B. R. Macdougall, *J. Phys. Chem. A*, 2012, **116**, 6771-6784.
4. M. Rajamathi, P. Vishnu Kamath and R. Seshadri, *J. Mater. Chem.*, 2000, **10**, 503-506.
5. M. Rajamathi, G. N. Subbanna and P. V. Kamath, *J. Mater. Chem.*, 1997, **7**, 2293-2296.
6. H. Ali-Löytty, M. W. Louie, M. R. Singh, L. Li, H. G. Sanchez Casalongue, H. Ogasawara, E. J. Crumlin, Z. Liu, A. T. Bell and A. Nilsson, *J. Phys. Chem. C*, 2016, **120**, 2247-2253.
7. K. Everaerts, J. D. Emery, D. Jariwala, H. J. Karmel, V. K. Sangwan, P. L. Prabhumirashi, M. L. Geier, J. J. Mcmorrow, M. J. Bedzyk and A. Facchetti, *J. Am. Chem. Soc.*, 2013, **135**, 8926-8939.
8. A. N. Mansour, *Surf. Sci. Spectra*, 1994, **3**, 239-246.
9. S. Klaus, Y. Cai, M. W. Louie, L. Trotochaud and A. T. Bell, *J. Phys. Chem. C*, 2015, **119**, 7243-7254.
10. Elly, Uzunova, Dimitar, Klissurski, Stoyan and Kassabov, *J. Mater. Chem.*, 1994.
11. M. Gong, Y. Li, H. Wang, Y. Liang, J. Z. Wu, J. Zhou, J. Wang, T. Regier, F. Wei and H. Dai, *J. Am. Chem. Soc.*, 2013, **135**, 8452-8455.
12. W. Ma, R. Ma, C. Wang, J. Liang, X. Liu, K. Zhou and T. Sasaki, *ACS Nano*, 2015, **9**, 1977-1984.
13. Y. Jia, L. Zhang, G. Gao, H. Chen, B. Wang, J. Zhou, M. T. Soo, M. Hong, X. Yan and G. Qian, *Adv. Mater.*, 2017, **29**.
14. Duan, Xue, Shao, Mingfei, Evans, David, G., Wang, Zixuan and Li, *Chem. Sci.*, 2015.
15. X. Guo, C. Guo, C. Wang, C. Li and X. Sun, *Nanoscale Res. Lett.*, 2014, **9**, 670.
16. C. Zhang, M. Shao, L. Zhou, Z. Li and M. Wei, *Acs Appl Mater Interfaces*, 1944, **8**, 33697-33703.
17. J. Chi, H. Yu, B. Qin, L. Fu, J. Jia, B. Yi and Z. Shao, *ACS Appl. Mater. Interfaces*, 2017, **9**, 464.
18. Y. Le, F. Y. Jing, Y. G. Bu, L. Yan and W. D. L. Xiong, *Angew. Chem. Int. Ed.*, 2018, **57**, 172-176.
19. L. Yu, H. Zhou, J. Sun, F. Qin, F. Yu, J. Bao, Y. Yu, S. Chen and Z. Ren, *Energy Environ. Ence*, 2017, **10**, 1820-1827.
20. X. Jia, Y. Zhao, G. Chen, L. Shang, R. Shi, X. Kang, G. I. N. Waterhouse, L. Z. Wu, C. H. Tung and T. Zhang, *Adv. Energy Mater.*, 2016, **6**, 1502585.
21. J. Zhang, J. Liu, L. Xi, Y. Yu, N. Chen, S. Sun, W. Wang, K. M. Lange and B. Zhang, *J. Am. Chem. Soc.*, 2018, **140**, 3876-3879.
22. Diaz-Morales, O., Ferrus-Suspedra, D and Koper, M. T. *Chem. Sci.*, 2016, **7**, 2639-2645.
23. Klaus, S., Cai, Y., Louie, M. W., Trotochaud, L., and Bell, A. T. *J. Phys. Chem. C*, 2015, **119**, 7243-7254.
24. Lee, S., Bai, L and Hu, X.. *Angew. Chem. Int. Ed.*, 2020, **59**, 8072-8077.
25. Grosvenor, A. P., Biesinger, M. C., Smart, R. S. C and McIntyre, N. S. *Surface Science*, 2006, **600**, 1771-1779.